Article

Immunity

Metabolic Profiling Using Stable Isotope Tracing Reveals Distinct Patterns of Glucose Utilization by Physiologically Activated CD8$^+$ T Cells

Graphical Abstract

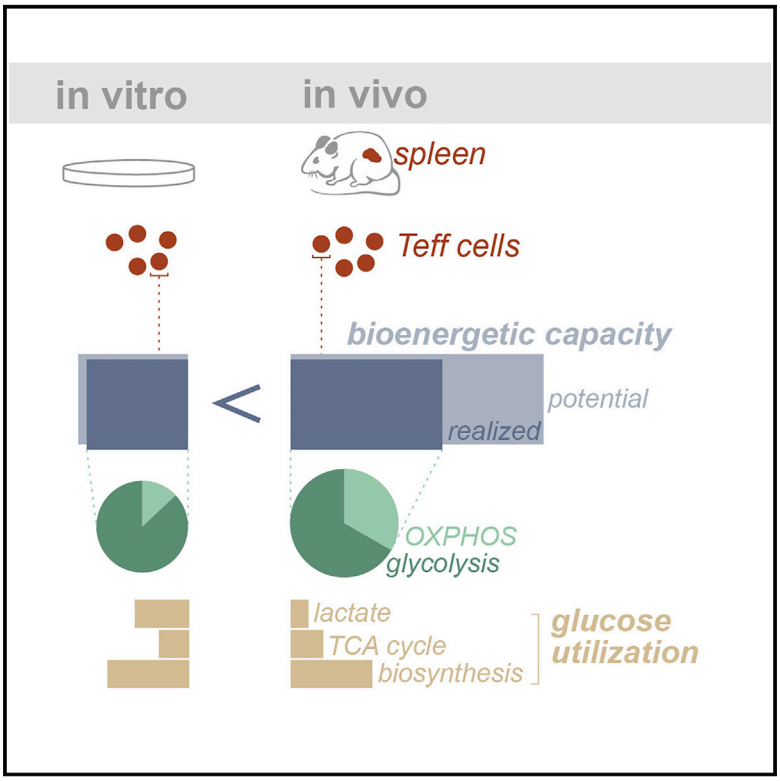

Authors

Eric H. Ma, Mark J. Verway, Radia M. Johnson, ..., Victor Chubukov, Thomas P. Roddy, Russell G. Jones

Correspondence

russell.jones@vai.org

In Brief

Although much is known about the metabolism of cultured T cells, how T cells use nutrients during immune responses *in vivo* is not well defined. Using ^{13}C-glucose isotope tracing in mice, Ma et al. demonstrate prominent use of glucose for anabolic metabolism by T cells *in vivo*. This work highlights the importance of studying T cell metabolism in a physiological environment.

Highlights

- Developed ^{13}C-infusion method for studying T cell metabolism *in vivo*
- T cell glucose use and bioenergetics differ between cell culture and mouse models
- Glucose metabolism in T cells changes dynamically over an immune response
- Glucose-dependent serine biosynthesis supports T cell proliferation *in vivo*

Ma et al., 2019, Immunity *51*, 856–870
November 19, 2019
https://doi.org/10.1016/j.immuni.2019.09.003

CellPress

CellPress

Immunity
Article

Metabolic Profiling Using Stable Isotope Tracing Reveals Distinct Patterns of Glucose Utilization by Physiologically Activated CD8$^+$ T Cells

Eric H. Ma,[1,2,3,9] Mark J. Verway,[2,3,9] Radia M. Johnson,[2,9] Dominic G. Roy,[2,3] Mya Steadman,[4] Sebastian Hayes,[4] Kelsey S. Williams,[1] Ryan D. Sheldon,[1] Bozena Samborska,[2,3] Penelope A. Kosinski,[4] Hyeryun Kim,[4] Takla Griss,[2,3] Brandon Faubert,[5] Stephanie A. Condotta,[2,6,7] Connie M. Krawczyk,[1,2,6] Ralph J. DeBerardinis,[5,8] Kelly M. Stewart,[4] Martin J. Richer,[2,6,7] Victor Chubukov,[4] Thomas P. Roddy,[4] and Russell G. Jones[1,2,3,10,*]

[1]Metabolic and Nutritional Programming, Center for Cancer and Cell Biology, Van Andel Institute, Grand Rapids, MI 49503, USA
[2]Goodman Cancer Research Centre, McGill University, Montreal, QC H3A 1A3, Canada
[3]Department of Physiology, McGill University, Montreal, QC H3G 1Y6, Canada
[4]Agios Pharmaceuticals, Cambridge, MA 02139, USA
[5]Children's Medical Center Research Institute, University of Texas Southwestern Medical Center, Dallas, TX 75390, USA
[6]Department of Microbiology and Immunology, McGill University, Montreal, QC H3G 1Y6, Canada
[7]Microbiome and Disease Tolerance Centre, McGill University, Montreal, QC H3G 1Y6, Canada
[8]Howard Hughes Medical Institute, The University of Texas Southwestern Medical Center, Dallas, TX 75390, USA
[9]These authors contributed equally
[10]Lead Contact
*Correspondence: russell.jones@vai.org
https://doi.org/10.1016/j.immuni.2019.09.003

SUMMARY

Naive CD8$^+$ T cells differentiating into effector T cells increase glucose uptake and shift from quiescent to anabolic metabolism. Although much is known about the metabolism of cultured T cells, how T cells use nutrients during immune responses *in vivo* is less well defined. Here, we combined bioenergetic profiling and ^{13}C-glucose infusion techniques to investigate the metabolism of CD8$^+$ T cells responding to *Listeria* infection. In contrast to *in vitro*-activated T cells, which display hallmarks of Warburg metabolism, physiologically activated CD8$^+$ T cells displayed greater rates of oxidative metabolism, higher bioenergetic capacity, differential use of pyruvate, and prominent flow of ^{13}C-glucose carbon to anabolic pathways, including nucleotide and serine biosynthesis. Glucose-dependent serine biosynthesis mediated by the enzyme Phgdh was essential for CD8$^+$ T cell expansion *in vivo*. Our data highlight fundamental differences in glucose use by pathogen-specific T cells *in vivo*, illustrating the impact of environment on T cell metabolic phenotypes.

INTRODUCTION

T cells are central players in adaptive immunity, mediating antigen-specific recognition and control of pathogens and cancer cells. Upon T cell receptor (TCR) engagement and appropriate co-stimulation, naive T (Tn) cells become activated and differentiate into T effector (Teff) cells essential for mediating protective immunity. Teff cell expansion is driven largely by changes in cellular metabolism (i.e., metabolic reprogramming) that support T cell growth, proliferation, and effector function (Geltink et al., 2018). Activated T cells increase expression of nutrient transporters (Macintyre et al., 2014; Sinclair et al., 2013) and enzymes involved in glycolysis and mitochondrial metabolism for ATP production and biosynthesis (Kishton et al., 2016; Ron-Harel et al., 2016; Tan et al., 2017; Wang et al., 2011). One of the prominent metabolic signatures of proliferating T cells *in vitro* is increased glucose uptake and lactate production, commonly known as the Warburg effect (MacIver et al., 2013; Pearce et al., 2013). Blocking glycolysis reduces effector function of both Teff and T memory (Tmem) cells (Cham and Gajewski, 2005; Chang et al., 2013; Gubser et al., 2013; Sukumar et al., 2013), highlighting the importance of metabolic reprogramming and nutrient availability for proper immune function.

Our understanding of immune cell metabolism has been aided by ^{13}C-based stable isotope labeling (SIL) techniques that facilitate tracing the metabolic fate of nutrients in cells and tissues (Jang et al., 2018; Klionsky et al., 2012). Metabolomic tracing techniques have helped identify key metabolic pathways that influence T cell function and expansion, including arginine (Geiger et al., 2016), acetate (Balmer et al., 2016), one-carbon metabolism (Ma et al., 2017; Ron-Harel et al., 2016), and glucose and glutamine (Blagih et al., 2015; Cham et al., 2008; Chang et al., 2013). One limitation of SIL studies *in vitro* is that immune cells are cultured under different, and often super-physiological, nutrient and oxygen concentrations than experienced *in vivo*, and this can directly influence nutrient use (Cantor et al., 2017). Infusion of ^{13}C-labeled metabolites into mice and humans has revealed differences in nutrient use by cells *in vivo* compared with *in vitro* culture (Davidson et al., 2016; Hensley et al., 2016; Hui et al., 2017; Sellers et al., 2015). T cells show similar metabolic plasticity when nutrients such as glucose are limited (Blagih et al., 2015; Ho et al., 2015; Qiu et al., 2019), illustrating that the nutrient environment

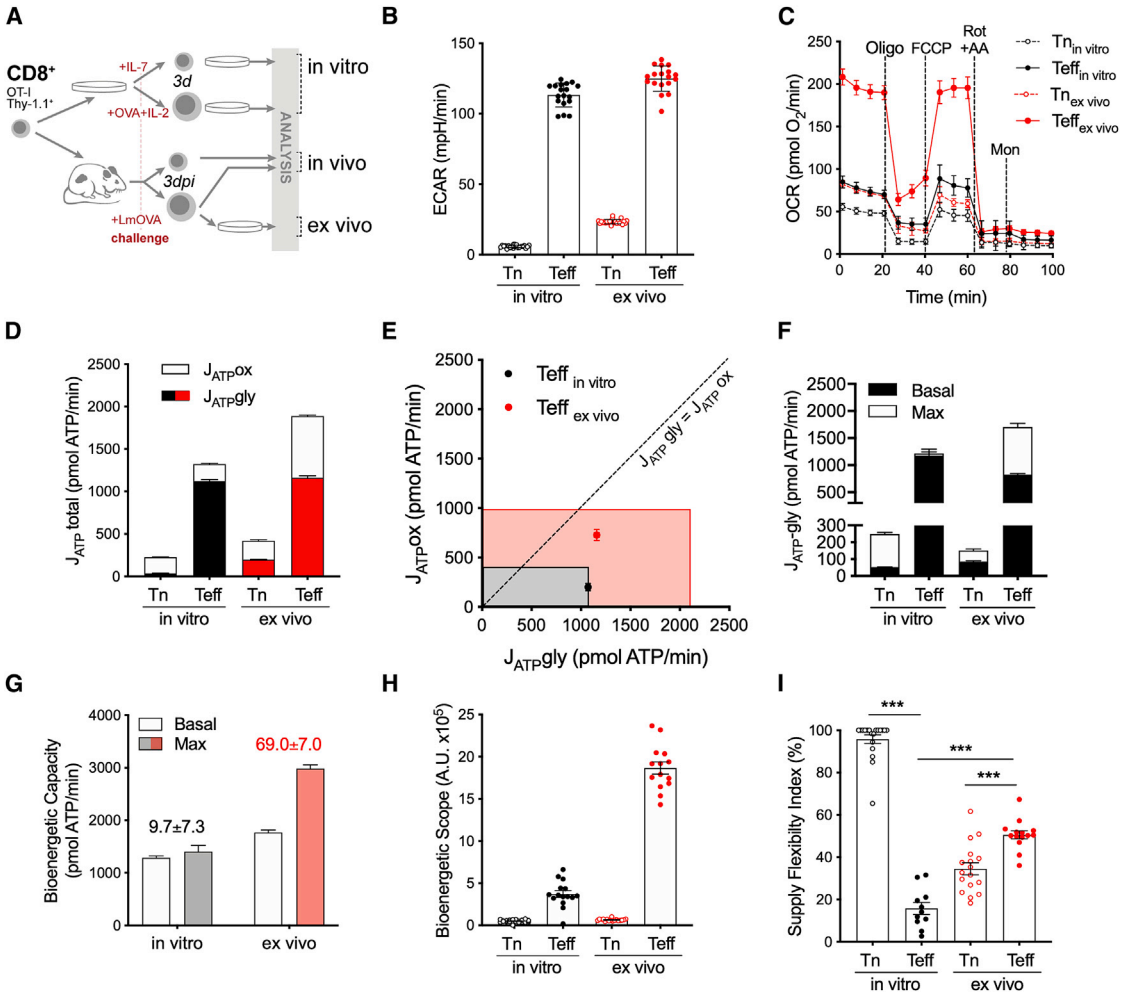

Figure 1. Physiologically Activated CD8⁺ T Cells Display Distinct Bioenergetic Profiles

(A) Schematic of the model system for *in vitro*, *in vivo*, and *ex vivo* OT-I T cell activation and analysis.

(B and C) ECAR (B) and OCR (C) of naive (Tn) or activated (Teff) CD8⁺ OT-I T cells cultured *in vitro* or *ex vivo* (mean ± SD, n = 16).

(D) ATP production rates (J_{ATP}) for Tn and Teff OT-I T cells cultured *in vitro* or *ex vivo* (n = 16).

(E) Bioenergetic capacity plot for OT-I Teff cells generated as in (D) (rectangle indicates maximum bioenergetic scope; symbol indicates basal ATP production rates [J_{ATP}ox and J_{ATP}gly]; n = 16).

(F) Basal and maximal glycolytic ATP production rates of Tn and Teff cells generated as in (D) (n = 4–12 per condition).

(G) Bioenergetic capacity of *in vitro* or *ex vivo* OT-I Teff cells generated as in (D) (numbers indicate spare bioenergetic capacity; n = 16).

(H and I) Bioenergetic scope (H) and supply flexibility index (I) for Tn or Teff cells generated as in (D) (n = 16).

can influence T cell metabolism. Evidence suggests that T cells may compete with surrounding tissues for nutrients to support their growth and proliferation (Chang et al., 2015; Ho et al., 2015), reinforcing the potential impact of environment *in vivo* on T cell metabolism.

In this study, we used a combination of bioenergetic profiling and ^{13}C-glucose-based SIL techniques to characterize the metabolism of CD8⁺ T cells responding to a pathogen (*Listeria monocytogenes*) *in vivo*. We found that CD8⁺ Teff cells activated *in vivo* displayed greater bioenergetic capacity and were more oxidative than Teff cells cultured *in vitro*. Moreover, we found that glucose use by CD8⁺ T cells changed dynamically over the course of an immune response and identified *de novo* serine biosynthesis as a key metabolic program for optimal T cell expansion *in vivo*. Our data highlight how the immune microenvironment *in vivo* influences metabolic requirements for T cells during an active immune response.

RESULTS

Physiologically Activated CD8⁺ T Cells Display Distinct Bioenergetic Profiles

To examine the metabolic differences between antigen-specific CD8⁺ T cells *in vitro* and *in vivo*, we conducted parallel studies using CD8⁺OT-I T cells expressing a TCR transgene specific for ovalbumin (OVA) (Figure 1A). These CD8⁺OT-I T cells were also congenic for CD90, expressing the Thy1.1 variant for rapid cell isolation using magnetic beads (see STAR Methods). For the purpose of this study, "*in vitro*" refers to experiments in which CD8⁺OT-I Tn cells were isolated from mice and then

activated with OVA peptide and IL-2 in standardized cell culture conditions to generate Teff cells (van der Windt et al., 2012; van der Windt et al., 2013) or maintained as Tn cell precursors by culture with IL-7 (Rathmell et al., 2001). "*In vivo*" refers to experiments in which $CD8^+$OT-I Thy1.1$^+$ T cells were adoptively transferred into C57BL/6 hosts followed by infection with *Listeria monocytogenes* expressing OVA (LmOVA), and then antigen-specific T cells were bead-isolated from spleens for immediate analysis by proteomics or metabolomics. "*Ex vivo*" refers to adoptive transfer experiments in which LmOVA-specific $CD8^+$OT-I Thy1.1$^+$ T cells isolated from spleens were subjected to short-term cell culture (<4 h) under standard culture conditions for additional analysis (Figure 1A).

Teff cells were isolated at 3 days post-infection (dpi), rather than at the peak of the Teff cell response when LmOVA has been cleared (6–8 dpi), to capture actively proliferating Teff cells. We followed the adoptive transfer guidelines recommended by the Immunological Genome Project Consortium (immgen.org) to study early-responding Teff cells *in vivo* (Best et al., 2013). This approach required us to transfer a large number of OT-I precursor cells (1–2 × 10^6) to obtain sufficient numbers of responding Teff cells for downstream analysis (Figure S1A). OT-I Teff cells generated using this protocol displayed the characteristic markers of early effector cells (EECs; KLRG1^{lo}CD127^{lo}) and were phenotypically similar to both *in vitro*-stimulated OT-I Teff cells and endogenous OVA-specific $CD8^+$ T cells (Figure S1B). *In vivo* OT-I Teff cells displayed other phenotypic characteristics of activation, including upregulation of cell surface markers CD69, CD25, and CD44 (Figure S1C) and acquisition of effector functions such as IFN-γ production (Figure S1D). Tn cells *in vivo* also displayed differences in CD69 and CD62L expression compared with Tn cells cultured *in vitro* (Figure S1C).

Using a Seahorse extracellular flux analyzer, we compared the bioenergetic profile of *in vitro*-activated OT-I T cells with those freshly isolated *ex vivo* at 3 dpi. Both *in vitro* and *ex vivo* Teff cells displayed characteristic increases in glycolysis associated with T cell activation, as demonstrated by a 6- to 10-fold increase in their extracellular acidification rate (ECAR) relative to Tn cells (Figure 1B). However, *ex vivo* Teff cells displayed a mitochondrial oxygen consumption rate (OCR) that was double that of their *in vitro* counterparts (Figure 1C).

To assess the contribution of glycolysis and oxidative phosphorylation (OXPHOS) to overall T cell bioenergetics, we converted ECAR and OCR measurements into glycolytic and oxidative ATP production rates using methodology developed by Mookerjee and Brand (Mookerjee et al., 2017). This allowed us to compare the contribution of glycolysis and OXPHOS to ATP production while correcting for the contribution of glycolysis and TCA cycle metabolism to ECAR. Although *in vitro* and *ex vivo* Teff cells showed similar rates of glycolytic ATP production (J_{ATP} *gly*), *ex vivo* Teff cells displayed greater overall ATP production because of their higher oxidative ATP production rate (J_{ATP} *ox*) (Figure 1D). *In vitro* Teff cells derived almost all of their ATP from glycolysis, displaying a glycolytic index (GI) consistent with the Warburg effect (Figure S1E). In contrast, *ex vivo* Teff cells derived ~1/3 of their ATP from OXPHOS (Figure S1E).

We next examined the bioenergetic capacity of $CD8^+$ T cells by measuring ATP production rates of T cells undergoing maximal glycolysis or OXPHOS. The latter was determined by measuring the J_{ATP} *ox* when T cells were cultured with the mitochondrial uncoupling agent FCCP, a similar approach as used to determine spare respiratory capacity (SRC) (van der Windt et al., 2012). Maximal glycolysis was measured as J_{ATP} *gly* under conditions of inhibited mitochondrial respiration and stimulation of plasma membrane Na^+ pumps (Mookerjee et al., 2017). As expected, Tn cells displayed lower overall bioenergetic capacity relative to Teff cells and were largely oxidative (Figure S1F). *In vitro* Teff cells operated at maximal glycolytic capacity (Figures 1E and 1F), consistent with their high GI, and displayed little spare bioenergetic capacity (SBC) (Figure 1G), congruent with previous reports (van der Windt et al., 2012). In contrast, *ex vivo* Teff cells operated far below their maximal oxidative and glycolytic capacity yet maintained greater overall ATP production (Figures 1E–1G). This translated to a 4- to 5-fold greater bioenergetic scope (i.e., the product of J_{ATP} *gly* and J_{ATP} *ox* rates) for *ex vivo* Teff cells compared with *in vitro*-activated T cells (Figure 1H). In addition to their higher bioenergetic scope, LmOVA-specific Teff cells analyzed *ex vivo* displayed a higher supply flexibility index (SFI), a measure of cellular bioenergetic plasticity (Mookerjee et al., 2017), compared with *in vitro*-activated Teff cells (Figure 1I). Thus, proliferating $CD8^+$ T cells challenged *in vivo* display a distinct bioenergetic profile that is characterized by increased oxidative ATP production, higher overall bioenergetic capacity, and increased flexibility to switch between ATP production pathways.

Proteomic and Metabolic Profiling Reveals Distinct Metabolic Features of Physiologically Activated $CD8^+$ T Cells

To characterize the metabolic profile of $CD8^+$ T cells responding to primary challenge with *Listeria in vivo*, we used parallel proteomic and metabolite profiling of Tn and Teff cells *in vitro* or isolated from LmOVA-infected mice as in Figure 1A. The magnetic bead-based isolation protocol used to isolate activated antigen-specific Thy1.1$^+$$CD8^+$OT-I (CD44^{hi}) and naive $CD8^+$ (CD44^{lo}) T cells from infected mice is summarized in Figure S2A (see STAR Methods). This protocol allowed us to purify Teff and Tn cell populations from the same mouse with greater than 90% purity (Figure S2B).

We compared protein expression in Tn versus Teff cells and found ~2,700 and ~2,200 differentially expressed proteins in our *in vitro* and *in vivo* datasets, respectively (differential abundance $\geq$ 50%, $p < 0.05$, $q < 0.25$; Tables S1, S2, S3, and S4). Approximately 27% of proteins significantly enriched in Teff cells were shared between datasets (Figure 2A). KEGG (Kyoto Encyclopedia of Genes and Genomes) analysis revealed that shared proteins in Teff cells were involved in pathways associated with cell proliferation (i.e., cell cycle, DNA replication, and purine and pyrimidine biosynthesis), mRNA translation (i.e., RNA transport, ribosome biogenesis, aminoacyl-tRNA biosynthesis), nucleotide excision repair, and TCR signaling (Figure 2B). KEGG analysis of proteins enriched in Tn cells showed distinct patterns of catabolic metabolism (i.e., glycosaminoglycan degradation, amino acid degradation, lipid metabolism) (Figure 2B), with lysosome and phagosome pathways featuring prominently. These data confirm previous reports of activation-induced T cell metabolic reprogramming (Kishton et al., 2016; Ron-Harel et al., 2016; Tan et al., 2017; Wang et al., 2011). *In vitro* and *in vivo* Teff cells

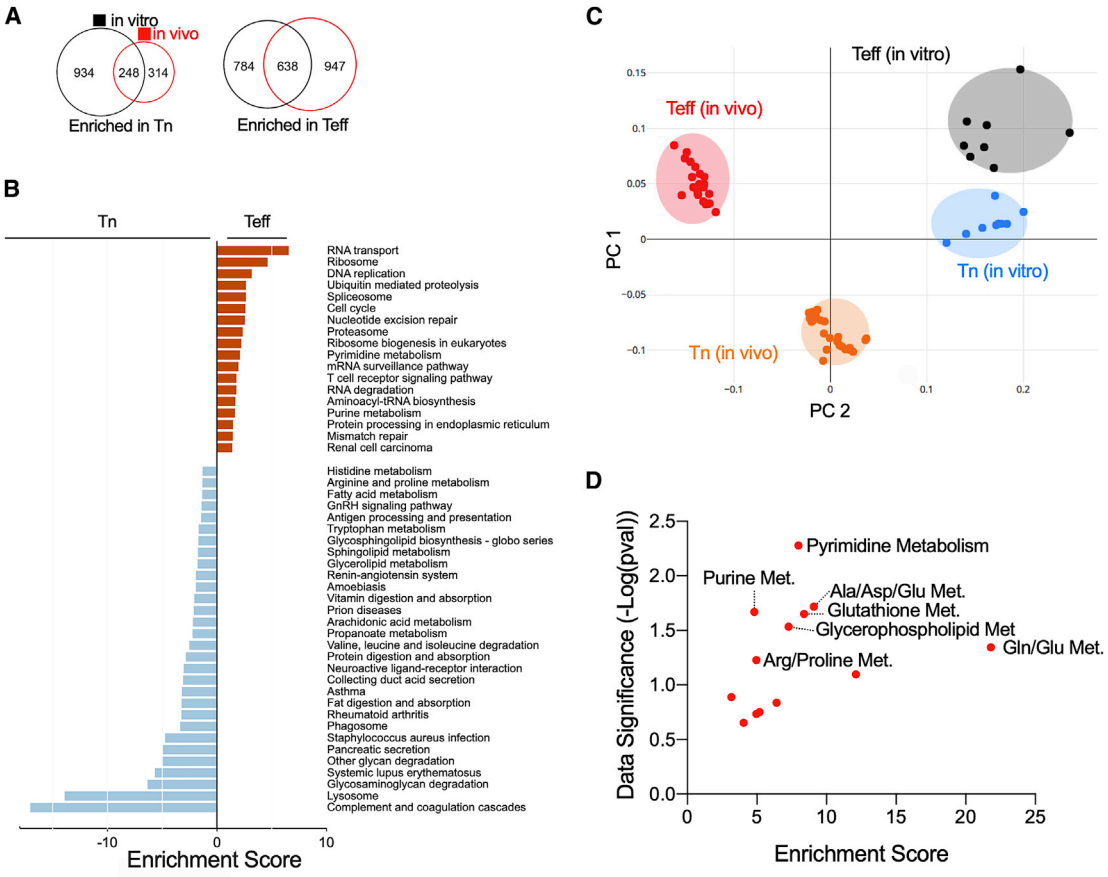

Figure 2. Proteomic and Metabolic Profiling Reveals Distinct Metabolic Features of Physiologically Activated CD8$^+$ T Cells

(A) Venn diagram illustrating differentially expressed proteins (relative peptide abundances) in CD8$^+$ OT-I T cells activated *in vitro* or responding to LmOVA *in vivo*. Left: proteins enriched in Tn cells relative to Teff. Right: proteins enriched in Teff cells relative to Tn.

(B) Enrichment scores for KEGG pathways significantly enriched in Teff and Tn cells *in vivo*, on the basis of proteomics analysis in Tables S1, S2, S3, and S4.

(C) Principal-component analysis (PCA) of total metabolite abundances from CD8$^+$ Tn and Teff cells activated *in vitro* or *in vivo*.

(D) Metabolic pathway enrichment analysis of metabolites enriched in Teff cells responding to LmOVA infection *in vivo*.

displayed similar general expression patterns for glycolytic and TCA cycle enzymes (Figure S2C). Exceptions included elevated Aldoc, Pkm1, and Idh1/2 expression in Teff cells stimulated *in vitro*, with Idh3 and Sdhc/d isoform expression featuring prominently *in vivo* (Figure S2C).

We next conducted targeted metabolomics on cellular T cell extracts using liquid chromatography-mass spectrometry (LC-MS). Recent work indicates that flow cytometry-based sorting can induce significant changes to the cellular metabolome (Binek et al., 2018; Llufrio et al., 2018). To assess the overall impact of our sorting protocol on cellular metabolites, we compared overall metabolite abundances in naive versus activated T cells following standard harvesting conditions (PBS wash) or a bead isolation procedure. Overall metabolite abundance increased in T cells upon activation, but metabolite abundance was higher in cells washed with PBS alone compared with cells that were bead-isolated (Figure S2D). Not all metabolite classes were affected equally by the isolation procedure. Cytosolic metabolite pools with high turnover (i.e., pyruvate, lactate, glutamine) as well as metabolite pools with lower abundance (i.e., α-ketoglutarate) displayed lower abundances following isolation (Figure S2E), and we detected these metabolites in isolation buffers post-isolation (Figure S2F). The abundance of several metabolites was stable following isolation (i.e., citrate, fumarate, histidine) (Figure S2E). For all experiments we directly compared T cells that had undergone the bead isolation procedure.

Principal-component analysis (PCA) revealed that the metabolite profiles of both Teff cells and Tn cells isolated from LmOVA-infected animals were distinct from their counterparts *in vitro* (Figure 2C), despite similar patterns of metabolic enzyme expression (Figure S2C). Metabolites enriched in physiologically activated T cells clustered in distinct KEGG pathways, including nucleotide (purine and pyrimidine) biosynthesis, glutathione metabolism, and glycerophospholipid metabolism (Figure 2D). Distinct pathways of amino acid metabolism were also observed, including glutamine and glutamate metabolism, aspartate metabolism, and arginine and proline metabolism (Figure 2D).

Stable Isotope Infusion Reveals Glucose Use Patterns in T Cells *In Vivo*

To analyze glucose use of CD8$^+$ T cells responding to LmOVA infection *in vivo*, we coupled our adoptive T cell transfer model

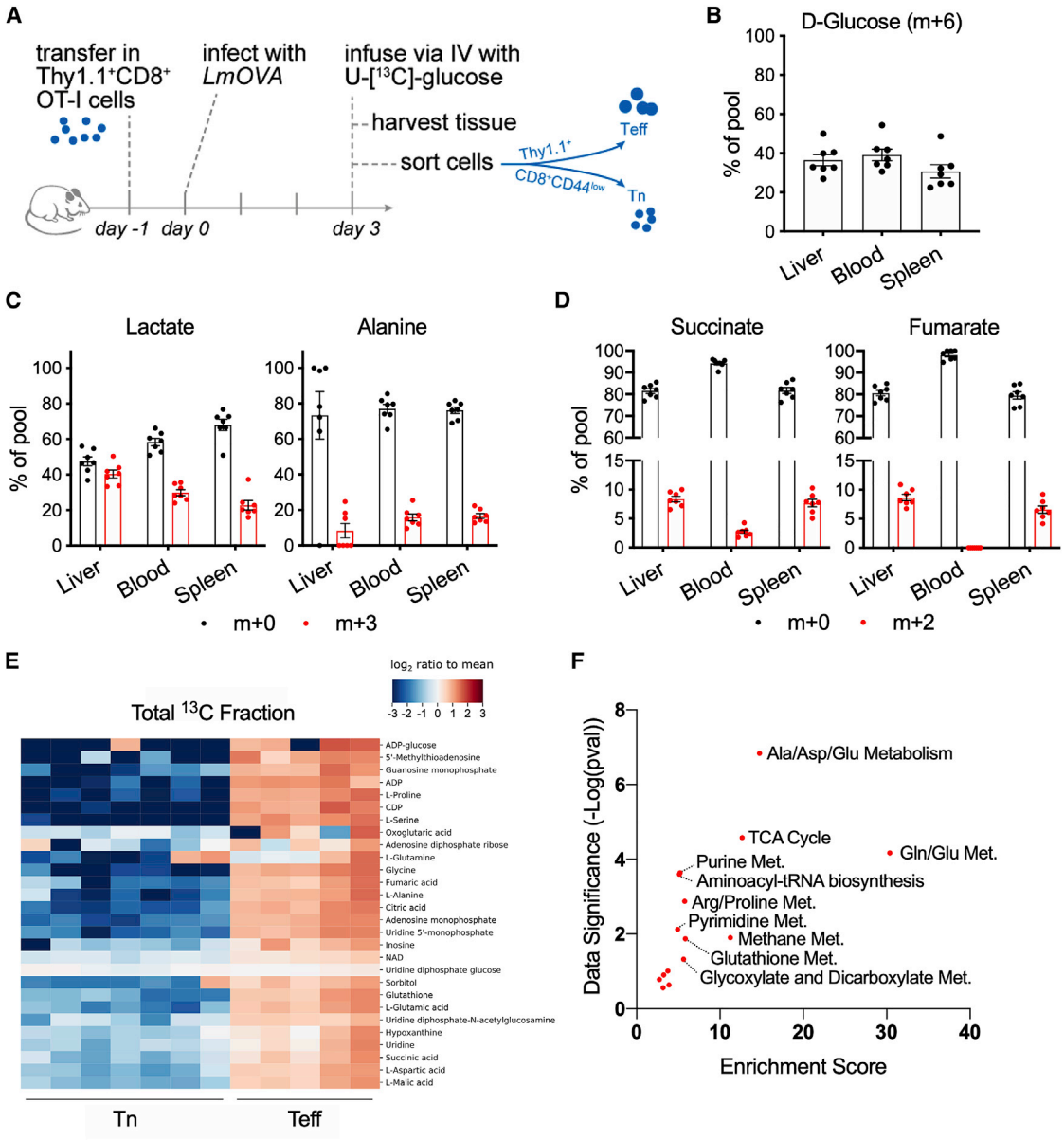

Figure 3. Stable Isotope Infusion Reveals Glucose Use Patterns in T Cells *In Vivo*

(A) Schematic of *in vivo* U-[^{13}C]-glucose infusion protocol.

(B) Liver, blood, and spleen glucose (m+6) enrichment following U-[^{13}C]-glucose IV infusion, as determined by LC-MS (mean ± SEM, n = 7).

(C and D) Labeling patterns of glycolytic (C) and TCA cycle (D) intermediates in liver, blood, and spleen following U-[^{13}C]-glucose infusion. For lactate and alanine, unlabeled (m+0) and fully labeled (m+3) isotopomers are shown. For succinate and fumarate, unlabeled (m+0) and prominent label (m+2, from one turn of the TCA cycle) isotopomers are shown (n = 7).

(E) Heatmap of significantly labeled metabolites ($p < 0.05$) in Teff and Tn cells after infusion. Data points reflect sum of abundance of all ^{13}C isotopologues.

(F) Metabolic pathway analysis of ^{13}C-labeled metabolites enriched in Teff cells from (E).

and rapid bead isolation procedure with established U-[^{13}C]-glucose infusion protocols (Hensley et al., 2016). Three days post-infection, anesthetized mice were infused intravenously with a bolus of U-[^{13}C]-glucose (12 mg/gBW), followed by continuous infusion (0.25 mg/gBW/min) for 120 min to achieve steady-state serum levels (Davidson et al., 2016; Hensley et al., 2016) after which antigen-specific (Thy1.1^{+}) and CD8^{+}Tn-cells were isolated from single-cell spleen preparations (Figure 3A). This infusion protocol allowed us to achieve ~40% isotopic enrichment of glucose m+6 in the blood and vascularized tissues, including the liver and spleen (Figure 3B), although other glucose isotopologues were also observed (Figure S3A). Analysis of metabolite abundances by LC-MS post-infusion revealed ^{13}C labeling in glycolytic pathway products (i.e., m+3 isotopologues of lactate, alanine, and pyruvate) (Figures 3C and S3B) and TCA cycle intermediates (i.e., m+2 isotopologues of citrate,

succinate, and fumarate) (Figures 3D and S3C). We also observed ^{13}C labeling in the TCA cycle-derived amino acids aspartate and glutamine (m+2 isotopologue) (Figure S3D). Overall, our infusion protocol yielded ^{13}C enrichment in spleen similar to labeling patterns found in other solid tissues such as lung (Davidson et al., 2016).

We next identified metabolites with significant enrichment in ^{13}C-glucose-derived carbon in Teff and Tn cells 3 dpi (Figure 3E). ^{13}C-glucose-enriched metabolites in Teff cells clustered into several pathways mirroring total metabolite abundances, including pyrimidine and purine metabolism, glutathione, glutamine, and alanine-aspartate-glutamate metabolism (Figure 3F). Significant ^{13}C enrichment from glucose was also observed in intermediates from the TCA cycle (citrate, α-ketoglutarate, succinate, fumarate, malate) and serine, glycine, one-carbon (SGOC) metabolism (serine, glycine) (Figure 3E).

We observed several trends when comparing ^{13}C-glucose-derived metabolites in T cells versus spleen (Figure S3E). First, UDP-glucose displayed the highest ^{13}C-glucose labeling among quantified metabolites in both Tn and Teff cells (Figure S3E). Second, a handful of metabolites (i.e., alanine, citrate, UDP-glucose) had high ^{13}C labeling in spleen, indicating possible production of these metabolites in other tissues such as the liver or high abundance in other immune cells. The percentage enrichment of these ^{13}C-containing metabolites in T cells increased upon activation, suggesting increased turnover in Teff cells. We also observed several ^{13}C-labeled metabolites with high enrichment in Teff cells contrasted with low enrichment in spleen, suggesting production from ^{13}C-glucose in Teff cells. These metabolites clustered into anabolic growth pathways including one-carbon metabolism (serine, glycine), the methionine cycle (SAM, SAH), and nucleotide biosynthesis (AMP, GMP, UMP) (Figure S3E).

Pyruvate Use by Teff Cells Differs *In Vivo*

Major fates of glucose-derived pyruvate in proliferating T cells include reduction to lactate by lactate dehydrogenase (Ldha), transamination to alanine by alanine transaminase (Alt/Gpt), or oxidation in the TCA cycle (Figure 4A). *In vitro* Teff cells displayed a high GI (Figure S1E) and glucose-to-lactate conversion (Figure 4B), consistent with a metabolic shift to the Warburg effect. In contrast, physiologically activated Teff cells operated at ~50% of maximal glycolysis (Figure 1E), suggesting other fates for glucose beyond lactate production. We next calculated the relative fractional enrichment of glucose-derived metabolites relative to spleen $^{13}C_6$-glucose abundances (for *in vivo* infusion) and cellular $^{13}C_6$-glucose abundances (for *in vitro* cultured cells). Consistent with previous reports (Angelin et al., 2017; Chang et al., 2013), Teff cells *in vitro* displayed increased fractional enrichment in lactate (m + 3) from ^{13}C-glucose upon activation (Figure 4C). In contrast, Teff cells labeled via *in vivo* infusion of ^{13}C-glucose displayed low labeling in lactate (<1% of total pool) and low overall fractional enrichment (Figure 4C). The low abundance of $^{13}C_3$-lactate in Teff cells was unexpected given the abundant lactate m+3 label observed in spleen tissue (Figure 3C). Unlike lactate, fractional enrichment of $^{13}C_3$-alanine was similar between Teff cells *in vitro* and *in vivo* (Figure 4C).

One possible reason for lower $^{13}C_3$-lactate abundance in Teff cells isolated from ^{13}C-glucose-infused mice was selective loss of $^{13}C_3$-lactate during bead isolation. We did, in fact, observe decreased m+3 labeling patterns for both lactate and pyruvate in T cells purified by bead isolation compared with normal extraction conditions (PBS wash) (Figure S4A). ^{13}C-glucose labeling in other metabolite pools (alanine, TCA cycle intermediates) was not affected by the bead isolation procedure (Figure S4A). Given these results, we compared the infusion tracing results with *ex vivo* ^{13}C tracing, in which $CD8^+$ OT-I cells isolated from LmOVA-infected mice (Figure 1A) were subjected to short-term culture in medium containing U-[^{13}C]-glucose. *In vitro*-activated Teff cells rapidly turned over $^{13}C_6$-glucose to $^{13}C_3$-lactate (~70% of pool labeled after 2 h), while LmOVA-specific Teff cells supplied $^{13}C_6$-glucose *ex vivo* displayed lower $^{13}C_3$-lactate production (30%–35% of pool labeled) in (Figure 4D). $^{13}C_3$-alanine production by Teff cells was similar between both conditions (Figure 4D).

Despite their phenotypic similarity to *in vitro*-activated Teff cells (Figures S1B–S1D), physiologically activated T cells at 3 dpi displayed 4- to 7-fold lower lactate abundance than their *in vitro* counterparts (Figure 4E). Moreover, *in vitro*-stimulated Teff cells maintained high production of $^{13}C_3$-lactate from glucose (>75% of total pool) over 4 days of culture compared with *ex vivo*-traced T cells (~35% of total pool) (Figure S4B). We next measured the rate of lactate production from ^{13}C-glucose by $CD8^+$ Teff cells by measuring abundance of $^{13}C_3$-lactate in culture medium over time. *Ex vivo* tracing of LmOVA-specific Teff cells revealed a ~50% lower lactate production rate than *in vitro*-activated Teff cells (1.4 compared with 2.7 μM/min) (Figure 4F). However, LmOVA-specific Teff cells converted to high lactate-producing cells after 24 h of culture *ex vivo* (Figure 4G), indicating that extensive tissue culture can alter the metabolic phenotype of T cells. This could be due to long-term IL-2 exposure, as culturing OT-I cells with IL-2 was sufficient to increase glucose-dependent lactate production, as well as increase glucose-dependent pyruvate entry into the TCA cycle (Figure S4C).

Pyruvate entry into the TCA cycle can occur via two distinct reactions. Pyruvate can be (1) decarboxylated by the Pdh complex to make acetyl-CoA, then enter the TCA cycle as citrate, or (2) carboxylated by pyruvate carboxylase (Pc) and enter the TCA cycle as oxaloacetate. $^{13}C_3$-pyruvate that enters as citrate contains two labeled carbons (i.e., m+2). Alternatively, $^{13}C_3$-pyruvate that enters as oxaloacetate (m+3) and combines with acetyl-CoA results in a three-labeled carbon citrate (i.e., m+3) (Figure 4A). *In vitro*-activated Teff cells displayed a prominent Pc activity signature, as evidenced by the enrichment of m+3 isotopologues of citrate, fumarate, and malate (Figure 4H). Conversely, both *in vivo*-traced (Figure 4H) and *ex vivo*-traced (Figure 4I) Teff cells revealed predominantly m+2-labeled TCA cycle intermediates. Mechanistically, *in vitro*-generated Teff cells displayed high Pc and low Pdh complex (Pdha1, Pdhb, and Pdhx) protein expression, which would support the observed m+3 labeling patterns in TCA cycle intermediates, while Teff cells responding to LmOVA *in vivo* displayed the inverse (low Pc and high Pdh expression) (Figure 4J). These data indicate key differences in pyruvate use by $CD8^+$ Teff cells responding to pathogen *in vivo*.

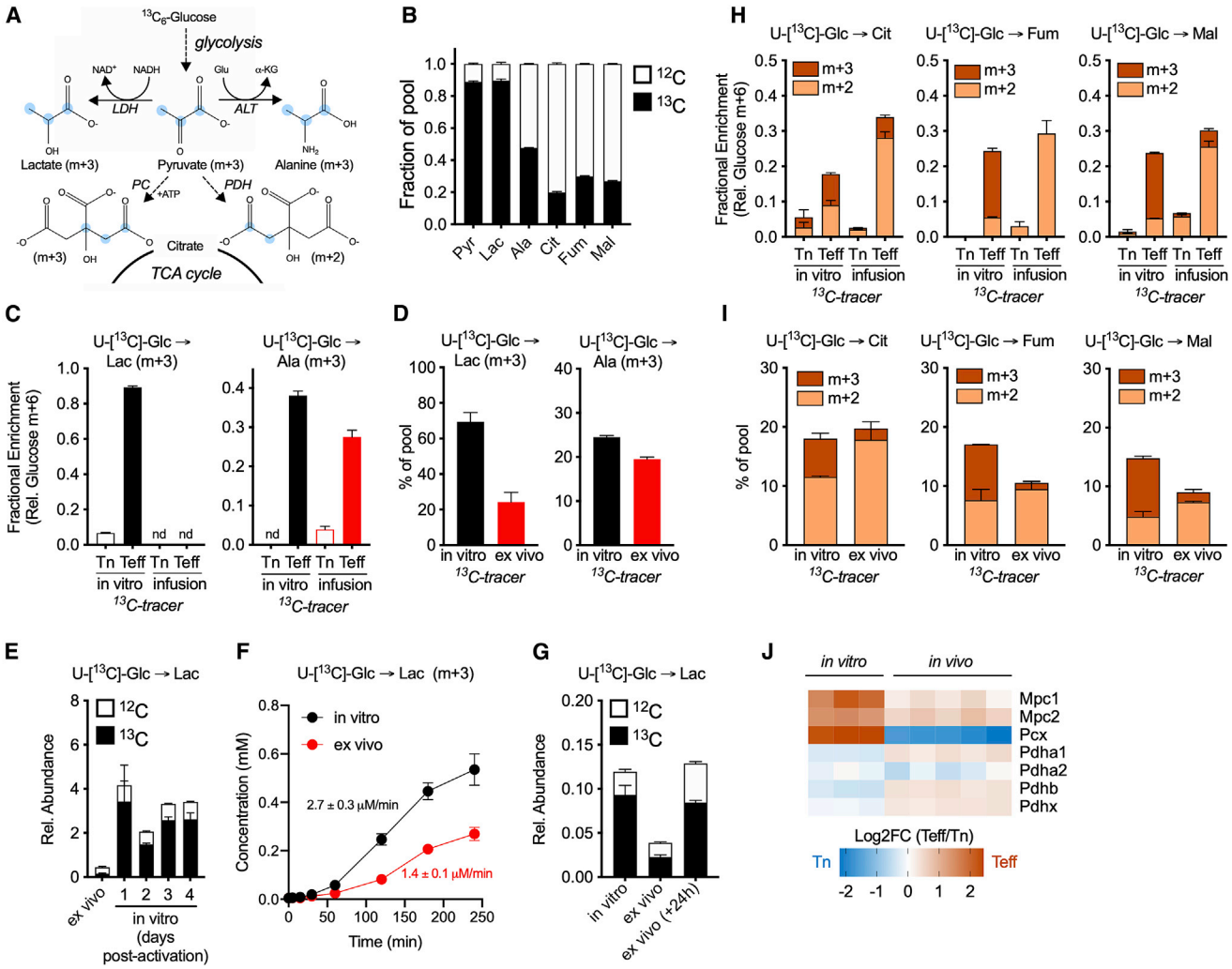

Figure 4. Pyruvate Use by Teff Cells Differs *In Vivo*

(A) Schematic of cytosolic pyruvate metabolism. Labeled carbon molecules from U-[^{13}C]-glucose are in blue. (ALT, alanine aminotransferase; LDH, lactate dehydrogenase; PC, pyruvate carboxylase; PDH, pyruvate dehydrogenase).

(B) Fractional enrichment of ^{13}C-glucose-derived glycolytic and TCA cycle intermediates for *in vitro*-activated Teff cells following 2 h culture with U-[^{13}C]-glucose.

(C) Fractional enrichment of intracellular ^{13}C-glucose-derived lactate and alanine for Tn and Teff cells cultured *in vitro* (black) or isolated following *in vivo* infusion (red), relative to $^{13}C_6$-glucose abundances in cells (for culture samples) or spleen (for infusion samples) (mean ± SEM; n = 3–6).

(D) Fractional enrichment of ^{13}C-lactate and ^{13}C-alanine (m+3 isotopomers) in OT-I Teff cells activated *in vitro* (black) or isolated from LmOVA-infected mice at 3 dpi (red). Cells were cultured with U-[^{13}C]-glucose for 2 h prior to extraction of intracellular metabolites (n = 3).

(E) Relative abundance of unlabeled (^{12}C) and labeled (^{13}C) intracellular lactate in OT-I Teff cells cultured as in (D) (n = 3).

(F) Time course of ^{13}C-lactate (m+3) excretion by OT-I Teff cells cultured as in (D). Concentration of ^{13}C-lactate in culture medium and rates of lactate production by OT-I Teff cells are shown (n = 3).

(G) Relative abundance of unlabeled (^{12}C) and labeled (^{13}C) lactate in OT-I Teff cells activated *in vitro*, isolated from LmOVA-infected mice 3 dpi (*ex vivo*), or LmOVA-specific cells cultured under *in vitro* conditions for 24 h (*ex vivo* +24 h). Cells were cultured with U-[^{13}C]-glucose for 2 h prior to extraction and quantification of intracellular metabolites (n = 3).

(H) Relative fractional enrichment of U-[^{13}C]-glucose-derived TCA cycle intermediates in Tn and Teff cells as in (C). Fractional enrichment of m+2 and m+3 isotopologues are shown (n = 3–6).

(I) U-[^{13}C]-glucose SIL into TCA cycle intermediates in Teff cells cultured as in (D). Fractional enrichment of m+2 and m+3 isotopologues are shown (n = 3).

(J) Ratio of relative protein abundance (Teff/Tn) for MPC, PC, and PDH complex components for OT-I T cells activated *in vitro* or isolated from LmOVA-infected mice (*in vivo*) (n = 3–5).

Glucose Contributes to Nucleotide and Nucleotide Sugar Biosynthesis in Teff Cells

We next examined additional pathways of glucose usage in Teff cells. Among the most abundant T cell metabolites containing a ^{13}C-glucose label was the nucleotide sugar UDP-glucose (Figure S3E). UDP-glucose and UDP-GlcNAc are nucleotide sugars generated immediately downstream of glucose-6-phosphate (Figure 5A) and serve as substrates for glycosyltransferase enzymes. *In vitro* Teff cells displayed accumulation of both UDP-glucose and UDP-GlcNAc relative to

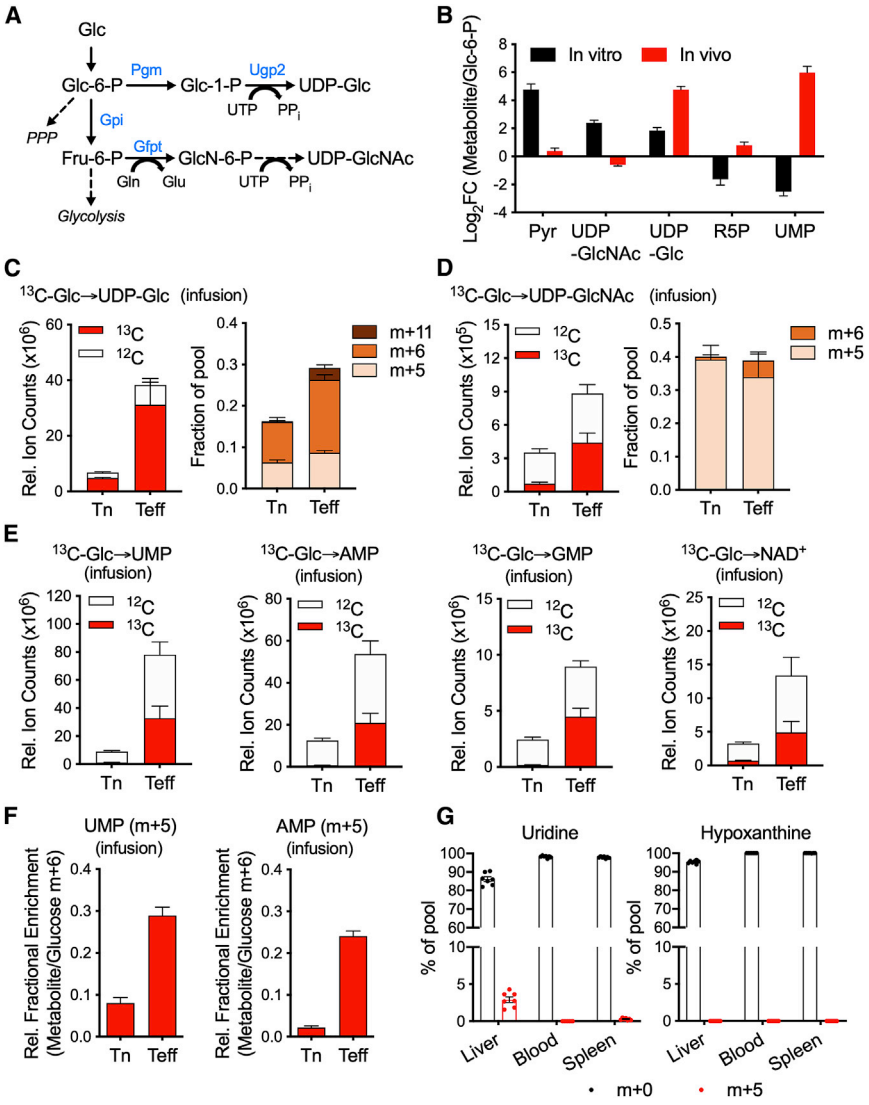

Figure 5. Glucose Contributes to Nucleotide and Nucleotide Sugar Biosynthesis in Teff Cells *In Vivo*

(A) Schematic of UDP-glucose and UDP-GlcNAc biosynthesis pathways. Key enzymes are in blue.

(B) Abundance of specific metabolites relative to Glc-6-P levels for $CD8^+$ Teff cells activated *in vitro* or *in vivo*.

(C) Relative abundance of unlabeled (^{12}C) and labeled (^{13}C) UDP-glucose (left) and SIL of major isotopologues of UDP-glucose (right) in Tn and Teff cells following 2 h U-[^{13}C]-glucose IV infusion (n = 6).

(D) Relative abundance of unlabeled (^{12}C) and labeled (^{13}C) UDP-GlcNAc (left) and SIL of UDP-GlcNAc isotopologues (right) in Tn and Teff cells, generated as in (C) (n = 6 or 7).

(E) Relative abundance of unlabeled (^{12}C) and labeled (^{13}C) nucleotides (UMP, AMP, GMP) and NAD^+ in Tn and Teff cells generated as in (C) (n = 6–7) (F) U-[^{13}C]-glucose SIL of UMP and AMP (m+5 isotopologue) in Tn and Teff cells relative to U-[^{13}C]-glucose abundance in spleen.

(G) Uridine and hypoxanthine (m+5 isotopologue) enrichment in liver, blood, and spleen, generated as in (C) (n = 7).

cellular glucose-6-phosphate (Figure 5B). *In vivo*, Teff cell-specific enrichment in UDP-glucose and UMP were observed (Figure 5B). The abundance of ^{13}C-labeled UDP-glucose in T cells *in vivo* increased ~5-fold upon activation (Figure 5C), with the isotopologue distribution shifting from predominantly m+6 (UTP combined with $^{13}C_6$-glucose) in Tn cells, to a combination of increased m+6 and emerging m+11 ($^{13}C_5$-ribose-containing UTP combining with $^{13}C_6$-glucose) (Figure 5C). Increased UDP-glucose synthesis in Teff cells may be favored because of high substrate abundance (i.e., glucose uptake), as expression of Ugp2, the key enzyme involved in UDP-glucose biosynthesis, did not change with activation (Figure S5A). Similar trends in UDP-glucose were observed *in vitro* (Figure S5B).

Another key nucleotide sugar for T cells is UDP-GlcNAc, the substrate for protein O-GlcNAcylation mediated by the enzyme O-GlcNAc glycosyltransferase (Ogt). Ogt is required for proper T cell development and Teff cell expansion (Swamy et al., 2016). Protein abundances of both Ogt and the enzymes that direct glucose-6-phosphate down the hexosamine biosynthesis pathway (Gfpt1, Gnpnat1) were elevated in Teff cells *in vivo* (Figure S5C). Similar to *in vitro* T cells (Figure S5D; Swamy et al., 2016), *in vivo* Teff cells displayed a ~5-fold increase in ^{13}C-glucose-labeled UDP-GlcNAc (Figure 5D). *In vitro*, UDP-GlcNAc production was sourced from both $^{13}C_6$-glucose and ^{13}C-glucose-labeled UTP as evidenced by prominent m+6 and m+11 isotopologues (Figure S5D). *In vivo*, UDP-GlcNAc was mostly the m+5 isotopologue (with some m+6) (Figure 5D), suggesting that turnover of the glucosamine moiety is relatively slow compared with the ribose moiety of UDP.

We next analyzed ^{13}C labeling patterns in UMP and AMP to assess glucose contribution to nucleotide biosynthesis. Nucleosides can be produced *de novo* (with the pentose phosphate shunt generating the nucleoside five-carbon sugar base) or obtained through salvage of existing nucleosides (from diet, circulation, or intracellular stores). In Teff cells, ^{13}C-glucose labeling was observed in purine (AMP, GMP), pyrimidine (UMP) nucleotides, and NAD^+, while Tn cells displayed minimal labeling (Figure 5E), consistent with production of these biomolecules by proliferating cells. Increased fractional enrichment of $^{13}C_5$-UMP and $^{13}C_5$-AMP (corresponding to fully labeled ribose) was observed in Teff cells compared with Tn cells (Figure 5F). However, labeled nucleosides in circulation (blood) or spleen, such as $^{13}C_5$-uridine and $^{13}C_5$-hypoxanthine, constituted less than 1% of the total metabolite pool in these tissues (Figure 5G). These data indicate that exogenous uptake of nucleotides is unlikely *in vivo*, but rather T cells actively produce nucleotides from glucose upon activation.

Pyrimidine and purine ^{13}C-labeling patterns in Teff cells also varied depending on environment (Figures S5E and S5F). *In vitro*, m+5 was the prominent isotopologue, corresponding to the formation of $^{13}C_5$-ribose from $^{13}C_6$-glucose. Additional m+6 and m+7 isotopologues in ADP likely correspond to SGOC-dependent contributions to the adenine ring (Labuschagne et al., 2014; Ma et al., 2017; Ron-Harel et al., 2016). In contrast, labeling of UMP and ADP was heterogeneous in Teff cells *in vivo* and included several low mass isotopologues (m+1,2,3,4) (Figures S5E and S5F). This may arise from the metabolism of other glucose isotopologues (Figure S3A) by Teff cells or SGOC-dependent biosynthesis of the nucleobase.

CD8$^+$ Teff Cell Metabolism Changes over the Course of Infection

We next compared the bioenergetic profile of CD8$^+$ T cells during early expansion (3 dpi) and late expansion (6 dpi, at the peak of the Teff cell response). CD8$^+$ Teff cells at 6 dpi displayed comparable CD44 expression but lower CD62L expression relative to Teff cells at 3 dpi (Figure S6A), with both displaying similar capacity to produce IFN-γ (Figure S6B) and granzyme B (Figure S6C). However, although Teff cells at 3 dpi were predominantly EECs (Figure S1B), Teff cells at 6 dpi were a mixed population of EECs (KLRG1^{lo}CD127^{lo}), short-lived effector cells (SLECs; KLRG1^{hi}CD127^{lo}), and memory precursor effector cells (MPECs; KLRG1^{lo}CD127^{hi}) (Figure S6D). We analyzed the OCR and ECAR of both Teff cell populations directly *ex vivo*. Although Teff cells isolated 3 dpi displayed characteristically higher OCR and ECAR relative to Tn cells, Teff cells isolated 6 dpi were more similar to Tn cells (Figures 6A and 6B). Teff cells at 3 dpi displayed a much larger bioenergetic space compared with Teff cells at 6 dpi, with late Teff cells displaying limited SBC with a more oxidative profile, similar to Tn cells (Figures 6C and 6D). This latter observation is consistent with previous characterization of Teff cells at the peak of the immune response to LmOVA (van der Windt et al., 2012). Notably, the overall ATP production capacity (Figure S6E) and bioenergetic scope (Figure 6E) of Teff cells dropped markedly between 3 and 6 dpi. Yet Teff cells at 6 dpi maintained a 2- to 3-fold greater bioenergetic scope than Tn cells (Figure 6E), indicating that they are not metabolically inert at this stage. Indeed, the SFI of Teff cells at 6 dpi indicated a greater bioenergetic plasticity than Teff cells at 3dpi (Figure S6F).

We next examined the metabolic profile of early and late Teff cells using *in vivo* $^{13}C_6$-glucose infusion in LmOVA-infected animals. PCA of total cellular metabolite abundance in Tn and Teff cells isolated from infected mice confirmed that early and late Teff cells were metabolically distinct, while Tn cells displayed a consistent metabolic profile over the course of infection (Figure 6F). Comparing differential $^{13}C_6$-glucose-labeling of intracellular metabolites in Teff cells between 3 and 6 dpi revealed that metabolites from anabolic growth pathways were reduced in late Teff cells (Figure 6G; Table S5). Pyruvate use by late Teff cells was similar to early Teff cells, with $^{13}C_6$-glucose-derived alanine and low lactate production (Figure S6G). Consistent with the lower OCR observed in Teff cells at 6 dpi (Figure 6A), we observed decreased fractional enrichment of $^{13}C_6$-glucose-derived TCA cycle metabolites in these cells compared with Teff cells at 3 dpi (Figure 6H). Glutamine and UDP-glucose were the only two metabolites preferentially ^{13}C-labeled in late Teff cells (Figures 6G and S6H). Overall, late Teff cells displayed patterns similar to Tn cells (Figure S6I), indicating that changes in glucose use in Teff cells precede contraction.

Glucose-Dependent Serine Biosynthesis Is Essential for Teff Cell Proliferation

We and others have identified serine as an essential metabolite for fueling T cell expansion, with extracellular serine used for purine nucleotide biosynthesis (Ma et al., 2017; Ron-Harel et al., 2016). Teff cells can either uptake serine from the extracellular environment or synthesize serine *de novo* from glucose (Figure 7A). Proteomic analysis of *in vitro*- and *in vivo*-activated OT-I CD8$^+$ T cells revealed similar increases in protein abundance for enzymes of the serine biosynthesis pathway (i.e., Phgdh, Psat1, and Psph), as well as enzymes that regulate one-carbon input from serine into the cytosolic and mitochondrial tetrahydrofolate cycles (i.e., Shmt1 and Shmt2, respectively) (Figure 7A). $^{13}C_6$-glucose-derived serine was in low abundance in circulation and spleen (<3% of total serine pool; Figure S7A) but was highly enriched in Teff cells *in vivo* (~15% of total pool; Figure 7B) and *in vitro* (~40% of total pool; Figure S7B). Input of one-carbon units from $^{13}C_6$-glucose-derived serine into the folate cycle was also detected in Teff cells, as evidenced by the increase in glycine (m+2) in Teff cells (Figures 7B and S7B). Fractional enrichment of $^{13}C_6$-glucose into common serine (m+1,2,3) and glycine (m+2) isotopologues was similar in both *in vitro*, *in vivo*, and *ex vivo* settings (Figures 7C and S7C), arguing that T cells produce serine *de novo* from glucose regardless of environment. Although bead isolation reduced overall serine and glycine abundances in T cells, ^{13}C labeling patterns were retained (Figure S7D).

Given the active engagement of glucose-dependent serine biosynthesis by Teff cells, we performed short hairpin RNA (shRNA)-mediated knockdown of Phgdh, the rate-limiting step of serine biosynthesis, in CD8$^+$ T cells. CD8$^+$ T cells were activated *in vitro*, followed by transduction with retrovirus expressing control or Phgdh-targeting shRNAs and isolation of transduced cells. Expression of shRNAs targeting *Phgdh* resulted in loss of Phgdh protein expression (Figure 7D) and reduced production of serine and glycine from $^{13}C_6$-glucose in CD8$^+$ T cells (Figure 7E). Neither silencing Phgdh nor removing exogenous serine and glycine affected expression of T cell activation markers CD44 or CD25 (Figure S7E). Silencing Phgdh reduced Teff cell proliferation to a similar extent as restricting serine and glycine in culture medium (Figure 7F). However, blocking endogenous serine biosynthesis (via Phgdh knockdown) in addition to restricting exogenous serine availability completely blocked Teff cell proliferation, despite ample abundance of glucose in the culture medium (Figure 7F).

Finally, we examined the role of Phgdh on CD8$^+$ T cell responses to LmOVA infection *in vivo*. Mice were maintained on a control or serine and glycine-free diet for 2 weeks prior to adoptive transfer of OT-I Thy1.1$^+$/Thy1.2$^+$ T cells transduced with control or Phgdh-targeting shRNAs. Infection with LmOVA followed 1 day later (Figure S7F). Analysis of splenocytes for the expansion of OVA-specific Thy1.1$^+$/Thy1.2$^+$ CD8$^+$ T cells 7 dpi revealed a significant reduction in both the percentage and number of OVA-specific CD8$^+$ Teff cells in mice maintained on

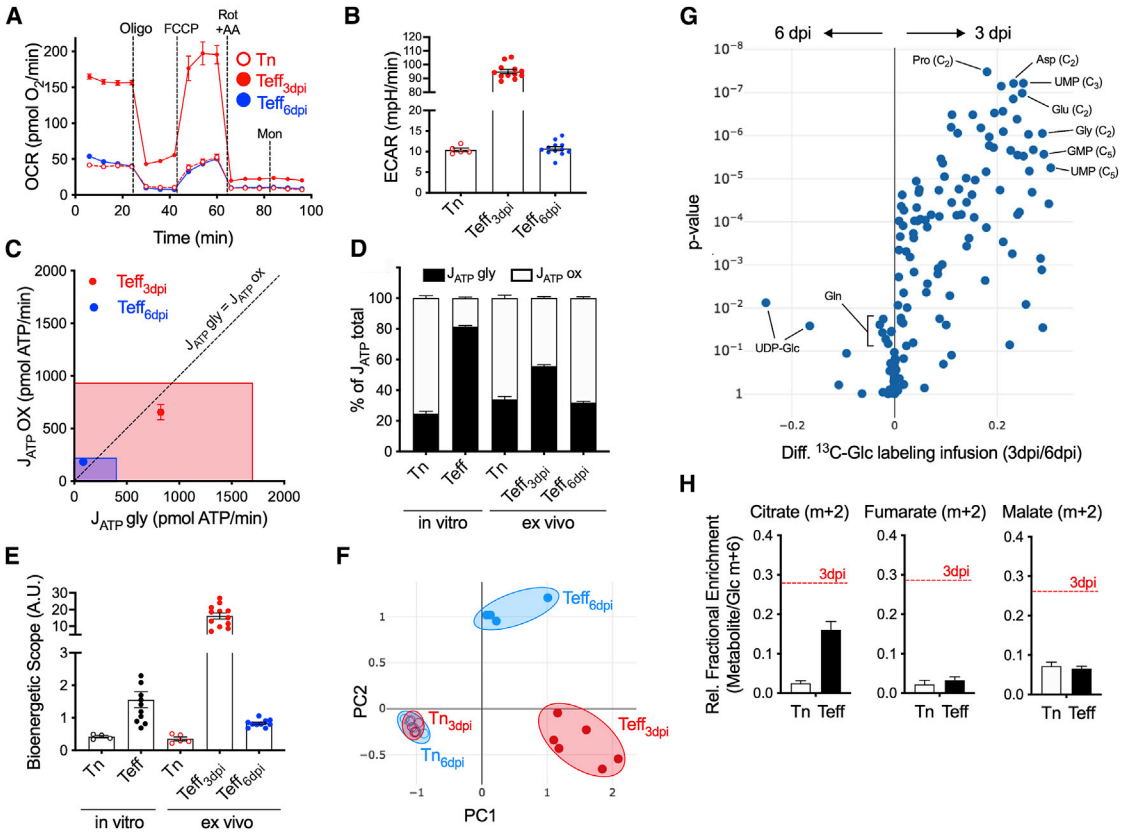

Figure 6. CD8⁺ Teff Cell Metabolism Changes over the Course of Infection

(A and B) OCR (A) and ECAR (B) of CD8⁺OT-I Tn or Teff cells isolated from LmOVA-infected mice at 3 or 6 dpi (n = 5–10).

(C) Bioenergetic capacity plot for OT-I Teff cells isolated as in (A). Rectangle indicates maximum bioenergetic scope; symbol indicates basal J_{ATP}ox and J_{ATP}gly (n = 10).

(D) Percentage of ATP generated from glycolysis versus OXPHOS for OT-I Teff cells cultured *in vitro* or analyzed *ex vivo* at 3 or 6 dpi.

(E) Bioenergetic scope of Tn and Teff cells cultured as in (D) (n = 5–10).

(F) PCA analysis of total metabolite abundances from OT-I Tn and Teff cells isolated as in (A).

(G) Volcano plot of differential U-[^{13}C]-glucose SIL in Teff cells isolated from mice at 3 dpi versus 6 dpi following 2 h infusion.

(H) U-[^{13}C]-glucose SIL of TCA cycle intermediates (m+2 isotopologues) in Tn and Teff cells 6 dpi generated as in (G) (red line, SIL in Teff cells at 3 dpi; n = 6).

a serine and glycine-restricted diet (Figures 7G and 7H), as previously reported (Ma et al., 2017). Silencing Phgdh resulted in a similar reduction in antigen-specific CD8⁺ T cell expansion compared with dietary serine restriction (Figures 7G and 7H). Combined serine restriction and silencing of Phgdh in CD8⁺ T cells resulted in >90% reduction in antigen-specific CD8⁺ T cell expansion *in vivo* (Figure 7H). Dietary serine and glycine restriction or Phgdh knockdown had no effect on the ability of Teff cells to produce IFN-γ but led to an overall reduction in the number of IFN-γ-producing Teff cells because of the reduced expansion of OVA-specific CD8⁺ Thy1.1⁺ T cells (Figure S7G). Our results indicate that serine-dependent one-carbon metabolism involving Phgdh is important for CD8⁺ T cell expansion *in vivo*.

DISCUSSION

Here we report the use of U-[^{13}C]-glucose IV infusions to assess CD8⁺ T cell metabolism *in situ* over the course of an immune response to a bacterial pathogen (*L. monocytogenes*). This approach allowed us to identify metabolic fates of glucose in both naive and activated T cells *in vivo*, examine differences from *in vitro* culture, and predict key metabolic pathways important for T cell function *in vivo*. Our data indicate key differences in glucose use by Teff cells *in vivo* compared with T cells proliferating *in vitro*. ^{13}C-glucose tracing results suggest lower lactate production and glucose oxidation by CD8⁺ Teff cells *in vivo* but that Teff cells adopt a Warburg-like metabolic phenotype with extensive culture *ex vivo*. We observed prominent signatures of glucose-dependent anabolism in early expanding CD8⁺ Teff cells characterized by ^{13}C-glucose labeling in nucleotide, nucleotide sugar, and SGOC metabolism. Moreover, we observed dynamic changes in glucose use by CD8⁺ T cells over the course of an immune response, with Teff cells at the peak of expansion displaying lower rates of glucose metabolism than CD8⁺ T cells at earlier phases of expansion. Our findings reinforce the pleiotropic nature of glucose as both a biosynthetic and bioenergetic substrate for proliferating T cells and highlight the impact of microenvironment on T cell nutrient use *in vivo*.

One challenge in studying immune cell metabolism is replicating the physiological conditions T cells encounter *in vivo*.

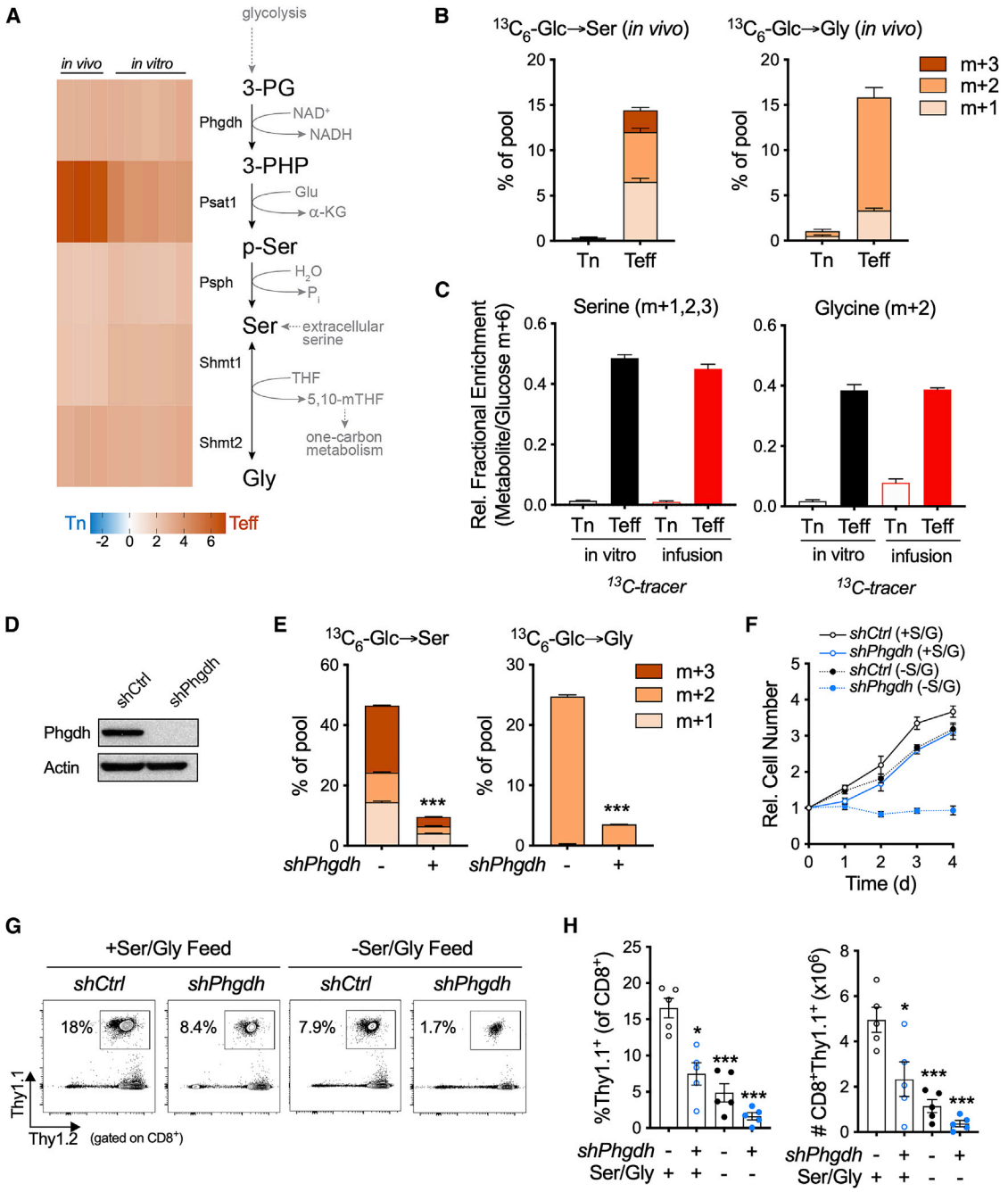

Figure 7. Glucose-Dependent Serine Biosynthesis Is Essential for Teff Cell Proliferation

(A) Abundance of SGOC enzymes in CD8$^+$OT-I Teff cells activated *in vitro* or *in vivo* (3 dpi). Data are relative to expression in Tn cells (mean ± SEM; n = 3–6).

(B) U-[^{13}C]-glucose SIL of serine and glycine in OT-I Tn and Teff cells *in vivo* (3 dpi) after 2 h infusion (n = 6).

(C) U-[^{13}C]-glucose SIL of serine and glycine in Tn and Teff cells cultured *in vitro* (black) or isolated following *in vivo* infusion (red) (n = 3–6).

(D) Immunoblot of Phgdh protein expression in OT-I Teff cells expressing control (*shCtrl*) or *Phgdh*-targeting (*shPhgdh*) shRNAs.

(E) U-[^{13}C]-glucose SIL of serine and glycine in *shCtrl*- (–) or *shPhgdh*-expressing (+) OT-I Teff cells (n = 3).

(F) Growth curve of *shCtrl*- or *shPhgdh*-expressing OT-I T cells cultured in medium with or without extracellular serine and glycine (n = 3).

(G) Representative flow cytometry plots showing abundance of OVA-specific Thy1.1$^+$/Thy1.2$^+$ OT-I T cells in the spleen of LmOVA-infected mice 7 dpi. Mice were maintained on control (+) or serine and glycine-free (–) chow 2 weeks prior to adoptive transfer of OT-I T cells expressing *shCtrl* or *shPhgdh* hairpins and then maintained on diets for the duration of the infection.

(H) Percentage and total number of OVA-specific (Thy1.1$^+$/Thy1.2$^+$) CD8$^+$OT-I T cells in spleens of LmOVA-infected mice 7 dpi (n = 5).

We attempted to control for these variables by using ^{13}C-glucose SIL via tail vein infusion, which allowed us to observe T cell metabolism *in situ* at different points over the course of infection. This approach revealed distinct metabolic states of CD8$^+$ Teff cells that change over the course of infection. Teff cells undergoing clonal expansion early in the immune response (3 dpi) were predominantly EECs and displayed prominent signatures of biosynthetic metabolism, including glucose-dependent nucleotide and SGOC metabolism. This metabolic program mirrored *in vitro*-activated CD8$^+$ T cells but contrasted with CD8$^+$ Teff cells at the peak of infection *in vivo* (6 dpi), which maintained robust effector function (i.e., IFN-γ production) yet largely lacked biosynthetic glucose metabolism. We see two possible interpretations; Teff cells at the peak of the immune response either (1) have lower metabolic demands than early effectors because of lower proliferation rates or (2) use fuel substrates other than glucose that are not modeled with our Seahorse experimental protocol or current infusion approaches. These data highlight two main points: (1) Teff cells can be segregated metabolically between early (proliferative) and late (non-proliferative) states, and (2) glucose may not be a major glycolytic or oxidative fuel in CD8$^+$ T cells at the peak of the T cell response *in vivo*. It must be noted that the late Teff cells we studied here constituted a mixed population of SLECs and MPECs. Future work will focus on whether these Teff cell subsets display distinct patterns of glucose use.

Upon antigen stimulation, T cells transition to an activated state marked first by increased growth ("blasting phase") and then by IL-2-dependent proliferation. Increased glycolysis is an early event that follows TCR triggering (Gubser et al., 2013). Current models suggest that proliferating Teff cells actively engage glycolysis for ATP production and effector function (Cham and Gajewski, 2005; Chang et al., 2013) but lack the metabolic flexibility and/or SRC required for long-lived Tmem cell function (van der Windt et al., 2012). There is strong evidence linking mitochondrial oxidative capacity to optimal T cell function and survival *in vivo* (Buck et al., 2016; Klein Geltink et al., 2017; Sukumar et al., 2016). However, our data indicate that SBC is a characteristic not just of Tmem cells but also of Teff cells. CD8$^+$ T cells cultured *in vitro* operated at their maximum bioenergetic capacity, displaying little spare glycolytic capacity or SRC, whereas early CD8$^+$ Teff cells *in vivo* displayed a more oxidative profile and could further increase their oxidative and glycolytic rate. We speculate that Teff cells adopt this metabolic flexibility to survive stressful conditions during clonal expansion, with T cells retaining the ability to rapidly increase ATP production through glycolysis when needed.

Our data provide insights into glucose use by CD8$^+$ Teff cells. First, our results suggest that aerobic glycolysis—the elevated conversion of pyruvate to lactate—is a less prominent metabolic program for Teff cells *in vivo*, as supported by their low production of ^{13}C-glucose-derived lactate. This is consistent with recent results in humans in which T cells display lower levels of aerobic glycolysis in response to vaccination (Klarquist et al., 2018). We speculate that high abundances of TCR, CD28, and IL-2 stimulation used for *in vitro* T cell culture, coupled with abundant and easy access to glucose, promote maximal glycolysis and lead to an imbalance in the cellular NAD$^+$/NADH ratio. T cells cultured *in vitro* may convert pyruvate to lactate out of necessity to regenerate NAD$^+$ and to diffuse the buildup of electrons from excessive NADH production (Sullivan et al., 2015). In support of this hypothesis, we observe that EECs isolated from LmOVA-infected mice converted to high lactate-producing cells within 24 h of culture *ex vivo*. *In vivo*, competition for nutrients and/or the use of glucose for other metabolic pathways (such as nucleotide and serine metabolism) may limit the production of NADH from glycolysis, reducing the need for Ldha-dependent buffering of cellular NAD$^+$/NADH.

Second, our data illustrate fundamental differences in glucose use by CD8$^+$ T cells depending on environment. *In vitro*, ^{13}C-glucose-derived pyruvate entered the TCA cycle primarily through Pc (as evidenced by increased m+3 signal in TCA cycle metabolites), while *in vivo* glucose entry was mediated mainly by pyruvate dehydrogenase (Pdh). Conversion of pyruvate to oxaloacetate by Pcconsumes ATP and thus may be favored only under energy-rich growth conditions seen *in vitro*. Our data also suggest that CD8$^+$ Teff cells dedicate a large portion of their glucose for cellular biosynthesis, particularly through metabolic pathways proximal to hexokinase, as opposed to using it primarily for ATP production. ^{13}C-glucose-derived carbon was readily detected in nucleotides such as UMP and AMP in Teff cells, with labeling patterns suggesting *de novo* synthesis. Increased use of glucose for synthesis of UDP-GlcNAc (a substrate used by cellular glycosyltransferases in T cells; Swamy et al., 2016) and UDP-Glc (an intermediate for glycan, glycosphingolipid, and glycogen biosynthesis) was also observed in CD8$^+$ EECs. We hypothesize that Teff cells may use non-glucose fuels such as glutamine (Lee et al., 2015) or acetate (Comerford et al., 2014; Mashimo et al., 2014) for mitochondrial oxidation to conserve glucose for the synthesis of complex macromolecules required for rapid T cell proliferation.

Third, serine biosynthesis emerged as a glucose-dependent metabolic node during T cell clonal expansion. Although proliferating T cells actively import and use exogenous serine (Ma et al., 2017; Ron-Harel et al., 2016), blocking glucose-dependent serine biosynthesis (via *Phgdh* knockdown) reduced T cell proliferation to the same extent as restricting extracellular serine availability. Reducing both *Phgdh* activity and exogenous serine abundance blocked T cell proliferation even under otherwise replete nutrient conditions, highlighting the importance of serine for optimal T cell function. Serine is a key contributor to multiple metabolic pathways, including purine and pyrimidine nucleotide biosynthesis via one-carbon metabolism, redox balance through contribution to glutathione biosynthesis, and lipid and protein synthesis (Gao et al., 2018; Labuschagne et al., 2014). The inability for just one source of serine (extracellular or glucose-derived) to support optimal T cell proliferation suggests compartmentalization of serine pools for cellular function.

By combining adoptive transfer and ^{13}C-glucose infusion techniques, we have characterized CD8$^+$ T cell metabolism over the course of an ongoing immune response. Advantages to this approach include the ability to study T cell metabolism *in situ* while ensuring physiological nutrient concentrations, cytokines, and inflammation, as well as the ability to assess metabolite abundances and SIL in both naive and activated T cells from the same mouse. Yet there are caveats to *in vivo* tracing that should be discussed. First, our infusion protocol consists of a

bolus of ^{13}C-glucose followed by a continuous infusion of tracer over 2 h, which can cause a transient spike in blood glucose and secretion of insulin into the bloodstream. Mice are also immobilized and sedated, which may alter the metabolism of certain nutrients or affect behavior of different immune cell subtypes (Liu et al., 2012). Non-invasive ^{13}C-glucose feeding approaches, which lack the time resolution offered by direct infusion, may present an alternate strategy (Sun et al., 2017). Fluorescence-activated cell sorting (FACS)-based cell sorting alters the metabolome of cells (Llufrio et al., 2018), as FACS-sorted cells are maintained for long periods of time in minimal buffers, which can lead to loss of cellular metabolites through diffusion. Although our method of magnetic bead isolation is faster than FACS-based cell sorting, it still takes ~30 min and can affect metabolite pools. For this reason, SIL in metabolites that have quick turnover, either through downstream incorporation or equilibrium with the extracellular environment (i.e., pyruvate and lactate), may be difficult to measure accurately. Conducting SIL on freshly isolated T cells may circumvent these issues, as activated T cells subjected to SIL *ex vivo* retained similar ^{13}C-glucose labeling patterns compared with those isolated following *in vivo* infusion.

To summarize, we report the use of ^{13}C-based SIL to assess T cell metabolism during an active immune response *in vivo*. Our data indicate that, similar to cancer cells (Davidson et al., 2016; Hensley et al., 2016), T cell metabolism is influenced by the microenvironment. This has implications for the type of competition T cells are likely to encounter *in vivo*, such as the tumor microenvironment. Competition for glucose between T cells and cancer cells has been reported (Chang et al., 2015). However, CD8$^+$ Teff cells and lung cancer cells adopt opposite metabolic profiles *in vivo*, with CD8$^+$ Teff cells producing little lactate and oxidizing glucose via PDH as opposed to PC (Davidson et al., 2016; Sellers et al., 2015). Thus, although T cells and tumor cells may compete for glucose in the tumor microenvironment, their use of glucose is likely to be different. Identifying and regulating the use of different substrates for T cell bioenergetics and/or biosynthesis may be a viable strategy for modulating immune responses.

STAR★METHODS

Detailed methods are provided in the online version of this paper and include the following:

- KEY RESOURCES TABLE
- LEAD CONTACT AND MATERIALS AVAILABILITY
- EXPERIMENTAL MODEL AND SUBJECT DETAILS
  - Mice
- METHOD DETAILS
  - T cell purification and culture
  - Flow cytometry, viability, and intracellular cytokine staining
  - Metabolic assays
  - Infection with L. monocytogenes
  - GC-MS analysis of ^{13}C metabolites
  - LC-MS analysis of ^{13}C metabolites
  - LC-MS metabolite identification and relative quantification
  - Proteomic analysis
  - *In vivo* infusion and CD90.1$^+$ cell isolation
- QUANTIFICATION AND STATISTICAL ANALYSIS
- DATA AND CODE AVAILABILITY

SUPPLEMENTAL INFORMATION

Supplemental Information can be found online at https://doi.org/10.1016/j.immuni.2019.09.003.

ACKNOWLEDGMENTS

We thank Shona Mookerjee; members of the Jones, Krawczyk, and Richer laboratories; and colleagues at Agios Pharmaceuticals for advice regarding the manuscript. We acknowledge technical assistance from Jeanie Wedberg, Michelle Minard, VAI Operations, and the Metabolomics and Flow Cytometry Core facilities at the VAI and McGill/GCRC. The GCRC Metabolomics Core Facility is supported by grants from the Canadian Foundation for Innovation (CFI), Canadian Institutes of Health Research (CIHR), and Terry Fox Research Institute (TFRI). We acknowledge salary support from the McGill Integrated Cancer Research Training Program (to E.H.M.), Fonds de la Recherche du Québec – Santé (FRQS; to E.H.M., D.G.R., and M.J.R.), and the CIHR (to D.G.R. and R.G.J.). This research was supported by grants from the CIHR (including MOP-142259 to R.G.J.) and funding from Agios Pharmaceuticals.

AUTHOR CONTRIBUTIONS

Experimental design and execution was conducted by E.H.M., M.J.V., D.G.R., M.S., S.H., B.S., P.A.K., H.K., S.A.C., C.M.K., M.J.R., K.M.S., T.P.R., and R.G.J. Bioinformatics and data analysis was conducted by E.H.M., R.M.J., R.D.S., and V.C. Data interpretation was performed by E.H.M., M.S., B.F., T.G., R.J.D., V.C., T.P.R., and R.G.J. The manuscript was written and edited by E.H.M., K.S.W., and R.G.J.

DECLARATION OF INTERESTS

S.H., P.A.K., H.K., K.M.S., V.C., and T.P.R. are employees and shareholders of Agios Pharmaceuticals. R.G.J. is a consultant to Agios Pharmaceuticals and is a shareholder and member of the scientific advisory board of Immunomet Therapeutics.

Received: March 7, 2019
Revised: June 11, 2019
Accepted: September 6, 2019
Published: November 19, 2019

REFERENCES

Angelin, A., Gil-de-Gomez, L., Dahiya, S., Jiao, J., Guo, L., Levine, M.H., Wang, Z., Quinn, W.J., 3rd, Kopinski, P.K., Wang, L., et al. (2017). Foxp3 reprograms T cell metabolism to function in low-glucose, high-lactate environments. Cell Metab. *25*, 1282–1293.e7.

Balmer, M.L., Ma, E.H., Bantug, G.R., Grählert, J., Pfister, S., Glatter, T., Jauch, A., Dimeloe, S., Slack, E., Dehio, P., et al. (2016). Memory CD8(+) T cells require increased concentrations of acetate induced by stress for optimal function. Immunity *44*, 1312–1324.

Best, J.A., Blair, D.A., Knell, J., Yang, E., Mayya, V., Doedens, A., Dustin, M.L., and Goldrath, A.W.; Immunological Genome Project Consortium (2013). Transcriptional insights into the CD8(+) T cell response to infection and memory T cell formation. Nat. Immunol. *14*, 404–412.

Binek, A., Rojo, D., Godzien, J., Ruperez, F.J., Nunez, V., Jorge, I., Ricote, M., Vazquez, J., and Barbas, C. (2018). Flow cytometry has a significant impact on the cellular metabolome. J. Proteome Res. *18*, 169–181.

Blagih, J., Coulombe, F., Vincent, E.E., Dupuy, F., Galicia-Vázquez, G., Yurchenko, E., Raissi, T.C., van der Windt, G.J., Viollet, B., Pearce, E.L., et al. (2015). The energy sensor AMPK regulates T cell metabolic adaptation and effector responses in vivo. Immunity *42*, 41–54.

Buck, M.D., O'Sullivan, D., Klein Geltink, R.I., Curtis, J.D., Chang, C.H., Sanin, D.E., Qiu, J., Kretz, O., Braas, D., van der Windt, G.J., et al. (2016). Mitochondrial dynamics controls T cell fate through metabolic programming. Cell *166*, 63–76.

Cantor, J.R., Abu-Remaileh, M., Kanarek, N., Freinkman, E., Gao, X., Louissaint, A., Jr., Lewis, C.A., and Sabatini, D.M. (2017). Physiologic medium rewires cellular metabolism and reveals uric acid as an endogenous inhibitor of UMP synthase. Cell *169*, 258–272.e17.

Cham, C.M., Driessens, G., O'Keefe, J.P., and Gajewski, T.F. (2008). Glucose deprivation inhibits multiple key gene expression events and effector functions in CD8+ T cells. Eur. J. Immunol. *38*, 2438–2450.

Cham, C.M., and Gajewski, T.F. (2005). Glucose availability regulates IFN-gamma production and p70S6 kinase activation in CD8+ effector T cells. J. Immunol. *174*, 4670–4677.

Chang, C.H., Curtis, J.D., Maggi, L.B., Jr., Faubert, B., Villarino, A.V., O'Sullivan, D., Huang, S.C., van der Windt, G.J., Blagih, J., Qiu, J., et al. (2013). Posttranscriptional control of T cell effector function by aerobic glycolysis. Cell *153*, 1239–1251.

Chang, C.H., Qiu, J., O'Sullivan, D., Buck, M.D., Noguchi, T., Curtis, J.D., Chen, Q., Gindin, M., Gubin, M.M., van der Windt, G.J., et al. (2015). Metabolic competition in the tumor microenvironment is a driver of cancer progression. Cell *162*, 1229–1241.

Chen, R., Bélanger, S., Frederick, M.A., Li, B., Johnston, R.J., Xiao, N., Liu, Y.C., Sharma, S., Peters, B., Rao, A., et al. (2014). In vivo RNA interference screens identify regulators of antiviral CD4(+) and CD8(+) T cell differentiation. Immunity *41*, 325–338.

Comerford, S.A., Huang, Z., Du, X., Wang, Y., Cai, L., Witkiewicz, A.K., Walters, H., Tantawy, M.N., Fu, A., Manning, H.C., et al. (2014). Acetate dependence of tumors. Cell *159*, 1591–1602.

Davidson, S.M., Papagiannakopoulos, T., Olenchock, B.A., Heyman, J.E., Keibler, M.A., Luengo, A., Bauer, M.R., Jha, A.K., O'Brien, J.P., Pierce, K.A., et al. (2016). Environment impacts the metabolic dependencies of Ras-driven non-small cell lung cancer. Cell Metab. *23*, 517–528.

Faubert, B., Vincent, E.E., Griss, T., Samborska, B., Izreig, S., Svensson, R.U., Mamer, O.A., Avizonis, D., Shackelford, D.B., Shaw, R.J., and Jones, R.G. (2014). Loss of the tumor suppressor LKB1 promotes metabolic reprogramming of cancer cells via HIF-1α. Proc. Natl. Acad. Sci. U S A *111*, 2554–2559.

Gao, X., Lee, K., Reid, M.A., Sanderson, S.M., Qiu, C., Li, S., Liu, J., and Locasale, J.W. (2018). Serine availability influences mitochondrial dynamics and function through lipid metabolism. Cell Rep. *22*, 3507–3520.

Geiger, R., Rieckmann, J.C., Wolf, T., Basso, C., Feng, Y., Fuhrer, T., Kogadeeva, M., Picotti, P., Meissner, F., Mann, M., et al. (2016). L-arginine modulates T cell metabolism and enhances survival and anti-tumor activity. Cell *167*, 829–842.e13.

Geltink, R.I.K., Kyle, R.L., and Pearce, E.L. (2018). Unraveling the complex interplay between T cell metabolism and function. Annu. Rev. Immunol. *36*, 461–488.

Griss, T., Vincent, E.E., Egnatchik, R., Chen, J., Ma, E.H., Faubert, B., Viollet, B., DeBerardinis, R.J., and Jones, R.G. (2015). Metformin antagonizes cancer cell proliferation by suppressing mitochondrial-dependent biosynthesis. PLoS Biol. *13*, e1002309.

Gubser, P.M., Bantug, G.R., Razik, L., Fischer, M., Dimeloe, S., Hoenger, G., Durovic, B., Jauch, A., and Hess, C. (2013). Rapid effector function of memory CD8+ T cells requires an immediate-early glycolytic switch. Nat. Immunol. *14*, 1064–1072.

Hensley, C.T., Faubert, B., Yuan, Q., Lev-Cohain, N., Jin, E., Kim, J., Jiang, L., Ko, B., Skelton, R., Loudat, L., et al. (2016). Metabolic heterogeneity in human lung tumors. Cell *164*, 681–694.

Ho, P.C., Bihuniak, J.D., Macintyre, A.N., Staron, M., Liu, X., Amezquita, R., Tsui, Y.C., Cui, G., Micevic, G., Perales, J.C., et al. (2015). Phosphoenolpyruvate is a metabolic checkpoint of anti-tumor T cell responses. Cell *162*, 1217–1228.

Hui, S., Ghergurovich, J.M., Morscher, R.J., Jang, C., Teng, X., Lu, W., Esparza, L.A., Reya, T., Le Zhan, Yanxiang Guo, J., et al. (2017). Glucose feeds the TCA cycle via circulating lactate. Nature *551*, 115–118.

Jang, C., Chen, L., and Rabinowitz, J.D. (2018). Metabolomics and isotope tracing. Cell *173*, 822–837.

Jones, R.G., Bui, T., White, C., Madesh, M., Krawczyk, C.M., Lindsten, T., Hawkins, B.J., Kubek, S., Frauwirth, K.A., Wang, Y.L., et al. (2007). The proapoptotic factors Bax and Bak regulate T Cell proliferation through control of endoplasmic reticulum Ca(2+) homeostasis. Immunity *27*, 268–280.

Kishton, R.J., Barnes, C.E., Nichols, A.G., Cohen, S., Gerriets, V.A., Siska, P.J., Macintyre, A.N., Goraksha-Hicks, P., de Cubas, A.A., Liu, T., et al. (2016). AMPK is essential to balance glycolysis and mitochondrial metabolism to control T-ALL cell stress and survival. Cell Metab. *23*, 649–662.

Klarquist, J., Chitrakar, A., Pennock, N.D., Kilgore, A.M., Blain, T., Zheng, C., Danhorn, T., Walton, K., Jiang, L., Sun, J., et al. (2018). Clonal expansion of vaccine-elicited T cells is independent of aerobic glycolysis. Sci. Immunol. *3*, eaas9822.

Klein Geltink, R.I., O'Sullivan, D., Corrado, M., Bremser, A., Buck, M.D., Buescher, J.M., Firat, E., Zhu, X., Niedermann, G., Caputa, G., et al. (2017). Mitochondrial priming by CD28. Cell *171*, 385–397.e11.

Klionsky, D.J., Abdalla, F.C., Abeliovich, H., Abraham, R.T., Acevedo-Arozena, A., Adeli, K., Agholme, L., Agnello, M., Agostinis, P., Aguirre-Ghiso, J.A., et al. (2012). Guidelines for the use and interpretation of assays for monitoring autophagy. Autophagy *8*, 445–544.

Krawczyk, C.M., Shen, H., and Pearce, E.J. (2007). Memory CD4 T cells enhance primary CD8 T-cell responses. Infect. Immun. *75*, 3556–3560.

Labuschagne, C.F., van den Broek, N.J., Mackay, G.M., Vousden, K.H., and Maddocks, O.D. (2014). Serine, but not glycine, supports one-carbon metabolism and proliferation of cancer cells. Cell Rep. *7*, 1248–1258.

Lee, C.F., Lo, Y.C., Cheng, C.H., Furtmüller, G.J., Oh, B., Andrade-Oliveira, V., Thomas, A.G., Bowman, C.E., Slusher, B.S., Wolfgang, M.J., et al. (2015). Preventing allograft rejection by targeting immune metabolism. Cell Rep. *13*, 760–770.

Liu, F.L., Chen, T.L., and Chen, R.M. (2012). Mechanisms of ketamine-induced immunosuppression. Acta Anaesthesiol. Taiwan. *50*, 172–177.

Llufrio, E.M., Wang, L., Naser, F.J., and Patti, G.J. (2018). Sorting cells alters their redox state and cellular metabolome. Redox Biol. *16*, 381–387.

Ma, E.H., Bantug, G., Griss, T., Condotta, S., Johnson, R.M., Samborska, B., Mainolfi, N., Suri, V., Guak, H., Balmer, M.L., et al. (2017). Serine is an essential metabolite for effector T cell expansion. Cell Metab. *25*, 345–357.

Macintyre, A.N., Gerriets, V.A., Nichols, A.G., Michalek, R.D., Rudolph, M.C., Deoliveira, D., Anderson, S.M., Abel, E.D., Chen, B.J., Hale, L.P., and Rathmell, J.C. (2014). The glucose transporter Glut1 is selectively essential for CD4 T cell activation and effector function. Cell Metab. *20*, 61–72.

MacIver, N.J., Michalek, R.D., and Rathmell, J.C. (2013). Metabolic regulation of T lymphocytes. Annu. Rev. Immunol. *31*, 259–283.

Maddocks, O.D., Berkers, C.R., Mason, S.M., Zheng, L., Blyth, K., Gottlieb, E., and Vousden, K.H. (2013). Serine starvation induces stress and p53-dependent metabolic remodelling in cancer cells. Nature *493*, 542–546.

Mashimo, T., Pichumani, K., Vemireddy, V., Hatanpaa, K.J., Singh, D.K., Sirasanagandla, S., Nannepaga, S., Piccirillo, S.G., Kovacs, Z., Foong, C., et al. (2014). Acetate is a bioenergetic substrate for human glioblastoma and brain metastases. Cell *159*, 1603–1614.

McGuirk, S., Gravel, S.P., Deblois, G., Papadopoli, D.J., Faubert, B., Wegner, A., Hiller, K., Avizonis, D., Akavia, U.D., Jones, R.G., et al. (2013). PGC-1α supports glutamine metabolism in breast cancer. Cancer Metab. *1*, 22.

Mookerjee, S.A., Gerencser, A.A., Nicholls, D.G., and Brand, M.D. (2017). Quantifying intracellular rates of glycolytic and oxidative ATP production and consumption using extracellular flux measurements. J. Biol. Chem. *292*, 7189–7207.

Pearce, E.L., Poffenberger, M.C., Chang, C.H., and Jones, R.G. (2013). Fueling immunity: insights into metabolism and lymphocyte function. Science *342*, 1242454.

Qiu, J., Villa, M., Sanin, D.E., Buck, M.D., O'Sullivan, D., Ching, R., Matsushita, M., Grzes, K.M., Winkler, F., Chang, C.H., et al. (2019). Acetate promotes T cell effector function during glucose restriction. Cell Rep. *27*, 2063–2074.e5.

Rathmell, J.C., Farkash, E.A., Gao, W., and Thompson, C.B. (2001). IL-7 enhances the survival and maintains the size of naive T cells. J. Immunol. *167*, 6869–6876.

Ron-Harel, N., Santos, D., Ghergurovich, J.M., Sage, P.T., Reddy, A., Lovitch, S.B., Dephoure, N., Satterstrom, F.K., Sheffer, M., Spinelli, J.B., et al. (2016). Mitochondrial biogenesis and proteome remodeling promote one-carbon metabolism for T cell activation. Cell Metab. *24*, 104–117.

Sellers, K., Fox, M.P., Bousamra, M., 2nd, Slone, S.P., Higashi, R.M., Miller, D.M., Wang, Y., Yan, J., Yuneva, M.O., Deshpande, R., et al. (2015). Pyruvate carboxylase is critical for non-small-cell lung cancer proliferation. J. Clin. Invest. *125*, 687–698.

Sinclair, L.V., Rolf, J., Emslie, E., Shi, Y.B., Taylor, P.M., and Cantrell, D.A. (2013). Control of amino-acid transport by antigen receptors coordinates the metabolic reprogramming essential for T cell differentiation. Nat. Immunol. *14*, 500–508.

Sukumar, M., Liu, J., Ji, Y., Subramanian, M., Crompton, J.G., Yu, Z., Roychoudhuri, R., Palmer, D.C., Muranski, P., Karoly, E.D., et al. (2013). Inhibiting glycolytic metabolism enhances CD8+ T cell memory and antitumor function. J. Clin. Invest. *123*, 4479–4488.

Sukumar, M., Liu, J., Mehta, G.U., Patel, S.J., Roychoudhuri, R., Crompton, J.G., Klebanoff, C.A., Ji, Y., Li, P., Yu, Z., et al. (2016). Mitochondrial membrane potential identifies cells with enhanced stemness for cellular therapy. Cell Metab. *23*, 63–76.

Sullivan, L.B., Gui, D.Y., Hosios, A.M., Bush, L.N., Freinkman, E., and Vander Heiden, M.G. (2015). Supporting aspartate biosynthesis is an essential function of respiration in proliferating cells. Cell *162*, 552–563.

Sun, R.C., Fan, T.W., Deng, P., Higashi, R.M., Lane, A.N., Le, A.T., Scott, T.L., Sun, Q., Warmoes, M.O., and Yang, Y. (2017). Noninvasive liquid diet delivery of stable isotopes into mouse models for deep metabolic network tracing. Nat. Commun. *8*, 1646.

Swamy, M., Pathak, S., Grzes, K.M., Damerow, S., Sinclair, L.V., van Aalten, D.M., and Cantrell, D.A. (2016). Glucose and glutamine fuel protein O-GlcNAcylation to control T cell self-renewal and malignancy. Nat. Immunol. *17*, 712–720.

Tan, H., Yang, K., Li, Y., Shaw, T.I., Wang, Y., Blanco, D.B., Wang, X., Cho, J.H., Wang, H., Rankin, S., et al. (2017). Integrative proteomics and phosphoproteomics profiling reveals dynamic signaling networks and bioenergetics pathways underlying T cell activation. Immunity *46*, 488–503.

van der Windt, G.J., Everts, B., Chang, C.H., Curtis, J.D., Freitas, T.C., Amiel, E., Pearce, E.J., and Pearce, E.L. (2012). Mitochondrial respiratory capacity is a critical regulator of CD8+ T cell memory development. Immunity *36*, 68–78.

van der Windt, G.J., O'Sullivan, D., Everts, B., Huang, S.C., Buck, M.D., Curtis, J.D., Chang, C.H., Smith, A.M., Ai, T., Faubert, B., et al. (2013). CD8 memory T cells have a bioenergetic advantage that underlies their rapid recall ability. Proc. Natl. Acad. Sci. U S A *110*, 14336–14341.

Vincent, E.E., Sergushichev, A., Griss, T., Gingras, M.C., Samborska, B., Ntimbane, T., Coelho, P.P., Blagih, J., Raissi, T.C., Choinière, L., et al. (2015). Mitochondrial phosphoenolpyruvate carboxykinase regulates metabolic adaptation and enables glucose-independent tumor growth. Mol. Cell *60*, 195–207.

Wang, R., Dillon, C.P., Shi, L.Z., Milasta, S., Carter, R., Finkelstein, D., McCormick, L.L., Fitzgerald, P., Chi, H., Munger, J., and Green, D.R. (2011). The transcription factor Myc controls metabolic reprogramming upon T lymphocyte activation. Immunity *35*, 871–882.

STAR★METHODS

KEY RESOURCES TABLE

REAGENT or RESOURCE	SOURCE	IDENTIFIER
Antibodies		
Monoclonal anti-mouse CD3, eBioscience Functional Grade, Purified	Invitrogen	Clone # 145-2C11; RRID: AB_468849
Monoclonal anti-mouse CD28, eBioscience Functional Grade, Purified	Invitrogen	Clone # 37.51; RRID: AB_468923
Rat monoclonal anti-mouse CD25	eBioscience	Clone # PC61.5
Rat monoclonal anti-mouse CD4	eBioscience	Clone # GK1.5
Rat monoclonal anti-mouse CD62L	eBioscience	Clone # MEL-14
Rat monoclonal anti-mouse IFN-gamma	eBioscience	Clone # XMG1.2
Rat monoclonal anti-mouse CD8	eBioscience	Clone # 53-6.7
Mouse monoclonal anti-mouse CD45.2	eBioscience	Clone # 104
Rat monoclonal anti-mouse CD127	BioLegend	Clone # A7R34; RRID AB_11218800
Hamster monoclonal anti-mouse KLRG1	eBioscience	Clone # 2F1; RRID AB_1311265
Rat monoclonal anti-mouse CD44	eBioscience	Clone # IM7
Rabbit polyclonal anti-human/mouse beta-actin	Cell Signaling	Cat # 4967; RRID AB_330288
Mouse monoclonal anti-mouse CD90.1 (Thy-1.1)	eBioscience	Clone # HIS51
Mouse monoclonal anti-mouse CD90.2 (Thy1-1.2)	eBioscience	Clone # 30-H12
Rabbit polyclonal anti mouse PHGDH Antibody	ThermoFisher Scientific	Cat # PA5-27578; RRID: AB_2545054
H-2Kb/OVA257 Tetramer	Baylor College of Medicine	N/A
Bacterial and Virus Strains		
Listeria monocytogenes rLM-OVA	van der Windt et al., 2012	N/A
Luciferase shRNA (LMPd-Amt backbone): AGCTCCCGTGAATT GGAATCCTAGTGAAGCCACAGATGTAGGATTCCAATTCAGCG GGAGCC	Chen et al., 2014 for vector backbone	N/A
Phgdh shRNA (LMPd-Amt backbone): tgctgttgacagtgagcgcgcact ggatgtgtttacagaatagtgaagccacagatgtattctgtaaacacatccagtgcatg cctactgcctcgga	This paper	N/A
Chemicals, Peptides, and Recombinant Proteins		
[U-^{13}C]-glucose	Cambridge Isotopes	Cat # CLM-1396
IMDM GlutaMAX	Thermo Fisher	Cat # 3198-022
Heat-inactivated FCS	Biochrom	Cat # 0115 – Lot# 1289W
Penicillin-streptomycin	Millipore	Cat # A2213
2-mercaptoethanol	GIBCO	Cat # 21985-023
recombinant murine IL-2	Peprotech	Cat # 212-12
recombinant murine IL-7	Peprotech	Cat # 217-17
Phorbol 12-myristate 13-acetate (PMA)	Sigma-Aldrich	Cat # P-8139
Ionomycin	Sigma-Aldrich	Cat # 10634
FCCP	Cayman	Cat # 15218
Oligomycin	Sigma-Aldrich	Cat # 1404-19-9
Rotenone	Cayman	Cat # 13955
Antimycin A	Sigma Aldrich	Cat # A8674
XF Base Medium Minimal DMEM without Phenol Red	Agilent	Cat # 103335-100
Glucose ≥ 99,5% D(+)	Roth	Cat # HN06.1
L-Glutamine	Biochrom AG	Cat # M11-004
Sodium Pyruvate	GIBCO	Cat # 11360-070
Poly-D-lysine hydrobromide	Sigma Aldrich	Cat # P6407

(*Continued on next page*)

Continued		
REAGENT or RESOURCE	SOURCE	IDENTIFIER
Recombinant murine IL-15	Peprotech	Cat # 3210-15
Fixable Viability Dye eFluor 506	eBioscience	Cat # 65-0866-14
Fixable Viability Dye eFluor 780	eBioscience	Cat # 65-0865-14
BD GolgiStop	BD Biosciences	Cat # 51-2092KZ
Foxp3/transcription factor staining buffer set	eBioscience	Cat # 00-5523-00
OVA(257-264) SIINFEKL peptide	Bio-Synthesis	custom
Critical Commercial Assays		
EasySep Mouse CD8+ T cell isolation kit	StemCell technologies	Cat # 19853
EasySep Mouse CD90.1 Positive Selection Kit	StemCell technologies	Cat # 18958
Seahorse XFe96 FluxPak	Agilent technologies	Cat # 102416-100
EasySep Mouse Naive CD8+ T cell isolation kit	StemCell technologies	Cat # 19858
Experimental Models: Cell Lines		
293T	ATCC	*Cat # CRL-3216*
Experimental Models: Organisms/Strains		
C57BL/6J mice	Charles River Laboratories	Cat # 027
OT-I mice	Jackson Laboratories	Cat # 003831
CD90.1 congenic mice	Jackson Laboratories	Cat # 000406
Software and Algorithms		
FlowJo 9.9.5	FlowJo	www.flowjo.com
GraphPad Prism V6 or V7	GraphPad Software	www.graphpad.com
El-Maven	Elucidata	https://elucidatainc.github.io/ElMaven/
Proteome Discoverer 2.1.0.81	Thermo Scientific	https://www.thermofisher.com/order/catalog/product/OPTON-30795

LEAD CONTACT AND MATERIALS AVAILABILITY

Additional information and request for resources and reagents should be directed to and will be made available by the Lead Contact, Russell G. Jones (russell.jones@vai.org). Plasmids generated in this study will be deposited to Addgene.

EXPERIMENTAL MODEL AND SUBJECT DETAILS

Mice

C57BL/6 (CD45.1 and CD45.2) were purchased from Charles River Laboratories. OT-I mice were purchased from The Jackson Laboratory (Bar Harbor, ME). Mice were bred and maintained under specific pathogen-free conditions at McGill University under protocols approved by the McGill University Animal Care Committee. For serine-restriction experiments, animals were fed Baker Purified Amino Acid Diet containing all essential amino acids plus serine, glycine, glutamine, arginine, cystine, and tyrosine, or a test diet lacking serine and glycine, as previously published (Maddocks et al., 2013). Animals were maintained on each diet for 2 weeks prior to infection and maintained on their respective diets until experimental endpoint. Experiments were performed using female mice between 6 and 20 weeks of age. Mice were kept in groups of 5 mice or less and had access to a pellet based feed and autoclaved reverse osmosis water.

METHOD DETAILS

T cell purification and culture

For *in vitro* $CD8^+$ mouse T cell isolation, $CD8^+$ T cells were purified from spleen and peripheral lymph nodes by negative selection (StemCell Technologies, Vancouver, BC, Canada). Cells were cultured in T cell medium (TCM) containing IMDM or custom IMDM for tracing studies (without serine, glycine, glucose, and glutamine) supplemented with 10% dialyzed FBS (Wisent, St. Bruno, QC), L-glutamine (Invitrogen, Chicago, IL), penicillin-streptomycin (Invitrogen), 2-ME (Sigma-Aldrich, St. Louis, MO), and glucose. L-serine (0.4 mM) and L-glycine (0.4 mM), were added to cell culture media as indicated. Naive $Thy1.1^+$ OT-I $CD8^+$ T cells were isolated and cultured *in vitro* with IL-7 or activated with OVA peptide with IL-2 for 3 days (*in vitro* growth conditions). In parallel, naive $Thy1.1^+$ OT-I $CD8^+$ T cells were adoptively transferred into $Thy1.2^+$ C57BL/6 mice by IV injection, followed by LmOVA infection one day later. Activated $Thy1.1^+$ OT-I $CD8^+$ T cells or naive $CD8^+$ T cells were isolated 3 days post infection (dpi) by magnetic bead

isolation and then analyzed immediately (*in vivo* conditions) or transferred to cell culture for additional analysis (*ex vivo* conditions). For activated T cells, purified T cells (1×10^6 cells/ml) were stimulated with plate-bound anti-CD3ε (clone 2C11) and anti-CD28 (clone 37.51) (eBioscience, San Diego, CA) and 50 U/ml IL2 (PeproTech, Rocky Hill, NJ). For naive $CD8^+$ mouse T cell cultures, naive $CD8^+$ T cells were purified from spleen and peripheral lymph nodes by negative selection (StemCell Technologies, Vancouver, BC, Canada). Isolated naive $CD8^+$ cells (1×10^6 cells/mL) were cultured in TCM supplemented with 5 ng/mL IL7. $CD8^+$ Tn or Teff cells isolated from LmOVA-infected mice were cultured immediately *ex vivo* in Seahorse XF medium (non-buffered DMEM 1640 containing 25mM glucose, 2mM L-glutamine, and 1mM sodium pyruvate) or TCM containing 10% dialyzed FBS. For T cell retrovirus transduction $CD8^+$ $CD90.1^+$ OT-I T cells were transduced with retrovirus 24 hours post activation and expanded up 1 day post-transduction in TCM for 2 days. Transduced T cells were sorted by FACS Aria and sorted T cells were kept in cultured overnight before T cell proliferation was measured by cell counts or transduced OT-T cells transferred into mice.

Flow cytometry, viability, and intracellular cytokine staining

Single-cell suspensions were surface stained with fluorescently conjugated Abs against murine CD4, CD8, CD44, CD90.1, CD90.2, CD62L, CD25, and CD69 (eBioscience). Cell viability was assessed using the Fixable Dye eFluor® 780 and 506 (eBioscience) following the manufacturer's protocol. Intracellular cytokine staining (ICS) for IFN-γ was performed as previously described (Blagih et al., 2015). Briefly, *in vitro* T cells were stimulated with PMA and ionomycin (Sigma-Aldrich) for 4 hr, with monensin added for the final 2 hr of stimulation, followed by ICS and flow cytometry. Flow cytometry was performed on LSR Fortessa (BD Biosciences) cytometers. Analysis was performed using with FlowJo software (Tree Star).

Metabolic assays

T cell oxygen consumption rate (OCR) and extracellular acidification rate (ECAR) were measured using a Seahorse XF96 Extracellular Flux Analyzer following established protocols (Blagih et al., 2015; Ma et al., 2017). In brief, activated T cells (2×10^5) were plated in poly-D-lysine-coated XF96 plates via centrifugation in XF medium. Cellular bioenergetics were assessed through the sequential addition of oligomycin (Oligo, 2.0 μM), fluoro-carbonyl cyanide phenylhydrazone (FCCP, 2.0 μM) for mitochondrial uncoupling, rotenone/antimycin A (Rot/AA, 2 μM) to inhibit mitochondrial respiration, and monensin (Mon, 10mM) to stimulate plasma membrane Na^+ pumps. Data were normalized to cell number. Bioenergetic capacity—or J_{ATP} total—was calculated as the sum of the glycolytic (J_{ATP}gly) and OXPHOS (J_{ATP}ox) ATP production rates at baseline (basal) or following FCCP and monensin treatment (max). Basal J_{ATP}gly was measured under standard T cell culture conditions (Glc, 25 mM; Gln, 4 mM), while maximal J_{ATP}gly was measured following ETC inhibition. Bioenergetic scope was calculated as the area of the rectangle defined in the bioenergetic capacity graph. Bioenergetics data analysis was based on protocols developed by Mookerjee et al. (2017) and is available for download at https://russelljoneslab.vai.org/tools.

Infection with L. monocytogenes

Mice were immunized IV with a sublethal dose of recombinant attenuated Listeria monocytogenes expressing OVA (LmOVA, 2×10^6 CFU) as previously described (Chang et al., 2013; Krawczyk et al., 2007). For OT-I adaptive transfer experiments (transduced cells), 5×10^3 $CD8^+$ OT-I T cells ($CD90.1^+$) were injected intravenously into C57BL/6 mice, followed by LmOVA infection 1 day later. Splenocytes were isolated from mice at 7 dpi and analyzed for the presence of OVA-specific $CD8^+$ T cells by CD90.1 (for adoptive transfer experiments of transduced T cells). Cytokine production by $CD8^+$ T cells was analyzed by ICS staining following peptide re-stimulation (OVA_{257}) as previously described (Jones et al., 2007). To generate *in vivo* activated $CD8^+$ T cells, for metabolomics, proteomics, and Seahorse bioanalyzer, $CD8^+CD90.1^+$OT-I T cells were injected intravenously into C57BL/6 mice, followed by LmOVA infection 1 day later. 2×10^6 or 5×10^4 cells were injected and isolated at 3 or 6 dpi respectively.

GC-MS analysis of ^{13}C metabolites

Gas chromatography coupled to mass spectrometry (GC-MS) was performed on T cells using previously described methods (Blagih et al., 2015; Griss et al., 2015; Vincent et al., 2015). Briefly, activated T cells were washed with PBS and re-cultured in TCM (lacking glucose and serine) containing 10% dialyzed FBS and uniformly labeled [^{13}C]-Glucose (Cambridge Isotope Laboratories). T cells (5×10^6 per well in 6 well plates) were cultured in ^{13}C-containing medium for up to 6 hours. For cellular media samples, 20 μL of media were taken at indicated time points and centrifuged to remove cells, with 10 μL of media used for metabolite analysis. Metabolites were extracted using ice cold 80% methanol, sonicated, and then D-myristic acid was added (750ng/sample) as an internal standard. Dried samples were dissolved in 30 μL methozyamine hydrochloride (10mg/ml) in pyridine and derivatized as tert-butyldimethylsily (TBDMS) esters using 70 μL N-(*tert*-butyldimethylsilyl)-N-methyltrifluoroacetamide (MTBSTFA) (Faubert et al., 2014).

For metabolite analysis, an Agilent 5975C GC/MS equipped with a DB-5MS+DG (30 m x 250 μm x 0.25 μm) capillary column (Agilent J&W, Santa Clara, CA, USA) was used. All data were collected by electron impact set at 70 eV. A total of 1 μL of the derivatized sample was injected in the GC in splitless mode with inlet temperature set to 280°C, using helium as a carrier gas with a flow rate of 1.5512 mL/min (rate at which myristic acid elutes at 17.94 min). The quadrupole was set at 150°C and the GC/MS interface at 285°C. The oven program for all metabolite analyses started at 60°C held for 1 min, then increased at a rate of 10°C/min until 320°C. Bake-out was at 320°C for 10 min. Sample data were acquired both in scan (1-600 m/z) and selected ion monitoring (SIM) modes. Mass isotopomer distribution for cellular metabolites was determined using a custom algorithm developed at McGill University (McGuirk

et al., 2013). Briefly, the atomic composition of the TBDMS-derivatized metabolite fragments (M-57) was determined, and matrices correcting for natural contribution of isotopomer enrichment were generated for each metabolite. After correction for natural abundance, a comparison was made between non-labeled metabolite abundances (^{12}C) and metabolite abundances which were synthesized from the ^{13}C tracer. Metabolite abundance was expressed relative to the internal standard (D-myristic acid) and normalized to cell number.

LC-MS analysis of ^{13}C metabolites

Metabolites were analyzed for relative abundance by high resolution accurate mass detection (HRAM) on two QExactive Orbitrap mass spectrometers (Thermo Fisher Scientific) coupled to Thermo Vanquish liquid chromatography systems. Separate instruments were used for negative and positive mode analysis. For negative mode analysis, an Acquity T3 HSS (1.8 μm, 2.1 mm x 150 mm) column (Waters, Eschborn, Germany) was used for chromatographic separation and the elution gradient was carried out with a binary solvent system. Solvent A consisted of 3% methanol, 10 mM tributylamine, and 15mM acetic acid in water (pH 5.0 ± 0.05) and solvent B was 100% methanol. A constant flow rate of 200 μL min^{-1} was maintained and the linear gradient employed was as follows: 0–2.5 min 100% A, 2.5–5 min increase from 0 to 20% B, 5–7.5 min maintain 80% A and 20% B, 7.5–13 min increase from 20 to 55% B, 13–15.5 min increase from 55 to 95% B, 15.5–18.5 min maintain 5% A and 95% B, 18.5–19 min decrease from 95 – 0% B, followed by 6 min of re-equilibration at 100% A. The heater temperature was set to 400°C and ion spray voltage was set to 2.75 kV. The column temperature was maintained at 25°C and sample volumes of 10 μL were injected. A 22-minute full-scan method was used to acquire data with *m/z* scan range from 80 to 1200 and resolution of 70,000. The automatic gain control (AGC) target was set at 1e6 and the maximum injection time was 500 ms. For positive mode analysis, an Atlantis T3 (3 μm, 2.1mm ID × 150mm) column (Waters) was used and the he elution gradient was carried out with a binary solvent system Solvent A consisted of 0.1% acetic acid and 0.025% heptafluorobutyric acid in water and solvent B was 100% acetonitrile. A constant flow rate of 400 μL min−1 was maintained and the linear gradient employed was as follows: 0–4 min increase from 0 to 30% B, 4–6 min from 30 to 35% B, 6–6.1 min from 35 to 100% B and hold at 100% B for 5min, followed by 5 min of re-equilibration. The heater temperature was set to 300°C and the ion spray voltage was set to 3.5 kV. The column temperature was maintained at 25°C and sample volumes of 10 μL were injected. An 11-minute full-scan method was used to acquire data with *m/z* scan range from 70 to 700 and resolution of 70,000. The automatic gain control (AGC) target was set at 1e6 and the maximum injection time was 250 ms. Instrument control and acquisition was carried out by Xcalibur 2.2 software (Thermo Fisher Scientific).

LC-MS metabolite identification and relative quantification

Full scan LC-MS data was centroided using vendor software, converted to mzXML format, and further analyzed using customized open-source software (El-Maven). Compounds were identified by *m/z* and retention time: expected *m/z* of de-protonated species was computed based on exact monoisotopic mass, and retention times were matched to those of previously analyzed pure standards and concurrently analyzed control samples. Peak intensities were calculated as the average of the three scans around the peak apex (“AreaTop”). Unless otherwise stated, abundances were normalized relative to $^{13}C_6$-glucose abundances in cells (for *in vitro*) or spleen (for infusion).

Proteomic analysis

Unless otherwise stated all chemicals were from Sigma Aldrich. All water and solvents were Optima LC/MS grade from Thermo Scientific.

Protein Extraction and Digestion: Cell pellets were lysed in 8M urea/50mM HEPES pH8.5 (Alfa Aesar) and treated with nuclease (Thermo Scientific) for 10 minutes at room temperature with constant shaking in a Thermomixer (Eppendorf). Lysates were reduced with 5 mM DTT for 30 minutes at 37C and cysteine residues alkylated with 15mM iodoacetamide for 30 minutes at room temperature in the dark. Excess iodoacetamide was quenched with 10mM DTT for 15 minutes at room temperature in the dark. Protein was extracted by methanol−chloroform precipitation and 2 × 1mL methanol washes. Pellets were dried and resuspended in 8M urea/50mM HEPES pH 8.5. Protein concentrations were measured by BCA assay (Thermo Scientific), diluted to 2M urea, and digested with LysC (Wako) in a 1:100 enzyme:protein ratio overnight at 30C. The next morning trypsin (Promega) was added to a final 1:100 enzyme:protein ratio for 6 h at 37C. Digests were acidified with 10% trifluoroacetic acid (TFA) to a pH ~2 and subjected to solid-phase extraction (SPE) with HyperSep Retain PEP Cartridges (Thermo Scientific). Peptides were resuspended in 200mM HEPES pH8.5/10% acetonitrile (ACN) and concentrations were measured by microBCA assay (Thermo Scientific).

Tandem Mass Tag Labeling: Isobaric labeling of peptides was performed using 10-plex tandem mass tag (TMT) reagents (Thermo Scientific). TMT reagents (0.8 mg) were dissolved in 41 μL of anhydrous ACN and 5 μL was added to 25μg of peptide. Samples were labeled for 2 hours at room temperature and quenched by the addition of hydroxylamine to 0.5% v/v for 15 minutes. Samples were pooled, acidified with 10% TFA to a pH ~2, and subjected to SPE. 1.08 mg of peptides from 36 protein digests labeled with TMT-131 was spiked into each 10-plex to normalize across 10-plex experiments. Sample usage and protein digests used in pool are described in Table S1.

Basic pH Reverse-Phase HPLC Fractionation: TMT-labeled peptides were subjected to orthogonal basic-pH reverse phase fractionation. Peptides were solubilized in buffer A 10mM ammonium bicarbonate pH 8.0/5% ACN and separated on a Biobasic C18 column (5μm particle size, 4.6mm ID, and 250mm length, Thermo Scientific) using an Ultimate 3000 HPLC (Thermo Scientific). A 44-min linear gradient from 12% to 36% ACN in 10 mM ammonium bicarbonate pH 8 (flow rate of 0.8 mL/min) separated the peptide

mixtures into a total of 96 fractions. The 96 fractions were consolidated into 24 samples in a checkerboard manner, acidified with TFA to pH ~2 and vacuum-dried. Each sample was re-dissolved in 20μL 5% formic acid (FA)/5% ACN and 2μL was analyzed by mass spectrometry.

Orbitrap Fusion Parameters: Spectra were acquired on an Oribtrap Fusion (Thermo Scientific) coupled to an Easy-nLC 1200 ultra-high pressure liquid chromatography (UHPLC) pump (Thermo Scientific). Peptides were separated on a 50 μM C18 EASYspray column (Thermo Scientific) using a 70 min, 8–28% ACN (constant 0.1% FA) gradient with a 300nL/min flow rate. MS1 spectra were collected in the Orbitrap at a resolution of 60,000, automated gain control (AGC) target of 5e5, and a max injection time of 100 ms. The 10 most intense ions were selected for MS/MS in a data dependent manner. Precursors were filtered according to charge state (2–6 z), monoisotopic peak assignment, and previously selected peaks were excluded using a dynamic window of 60 s with a mass error ± 10 ppm. MS2 precursors were isolated with a quadrupole mass filter set to a width of 0.5 m/z and detected in the ion trap operated at Rapid scan rate. MS2 spectra were collected at an AGC of 1e4, max injection time of 150ms, and CID collision energy of 35%. Synchronous-precursor-selection (SPS) was enabled to include the top 10 MS2 fragment ions for MS3 analysis in the Orbitrap at a resolution of 60,000, automated gain control (AGC) target of 5e5, and a max injection time of 250ms. 50% HCD collision energy was used to ensure TMT reporter detection.

Data Processing: All .RAW files were processed using Proteome Discoverer 2.1.0.81. MS2 spectral assignment was performed using the SEQUEST algorithm using Uniprot mouse reference proteome and a list of known contaminants (CRAPome.org). Mass tolerances were set to 10 ppm for precursor ions, 0.6 Da for MS2 ions, and 20 ppm for MS3 reporter ions. MS2 false discovery rate (FDR) of less than 1% was calculated using the Percolator algorithm. Reporter ion intensities were adjusted to correct for the isotopic impurities of the different TMT reagents (manufacturer specifications). TMT tags on peptide N termini/lysine residues (+229.162932 Da) and carbamidomethylation of cysteine residues (+57.02146 Da) were set as static modifications, and methionine oxidation (+15.99492 Da) was set as a variable modification. Signal-to-noise values for all peptides were summed within each TMT channel, and each channel was scaled according to the highest channel sum so that the sum abundance of each channel is equal. Peptides were filtered for a minimum sum signal-to-noise value of 160 across all 10 channels. Quantitation data from razor peptides were excluded, and only unique peptides were used for protein quantitation.

In vivo infusion and CD90.1$^+$ cell isolation

CD8$^+$CD90.1$^+$OT-I T cells were adoptively transferred into C57BL/6 mice, followed by infection with LmOVA one day later. Infected mice were infused via tail vein with U-[^{13}C]-glucose (Cambridge Isotope Laboratories, Andover, MA) dissolved in saline at 3 or 6 dpi. Mice were fasted overnight prior to tail vein infusion. Mice were anesthetized by i.p. injection (50uL for mice weighing 15-20 g) with a chemical cocktail of Ketamine (50mg/mL), Xylazine (10mg/mL), and Acepromazine (2mg/mL) and kept on a heating pad for the duration of the infusion process. A bolus of 0.6 mg U-[^{13}C]-glucose/g mice was given followed by a continuous infusion at 0.125 uL/min/g mice weight for a duration of 120 min. At the end of the infusion, blood was collected by cardiac puncture. Following blood collection, a lobe of liver and a piece of spleen were collected and flash frozen in liquid nitrogen and kept at −80°C. The rest of the spleen was turned into a single cell suspension, filtered through a 0.75 μm filter, and pelleted. The cell pellet was resuspended in 4 mL of EasySep buffer (PBS with 2% FBS and 1mM EDTA) and volume split equally for CD90.1$^+$ isolation (EasySep Mouse CD90.1 Positive Selection Kit) and naive CD8$^+$ T cell isolation (EasySep Mouse Naive CD8+ T cell isolation kit).

Cell isolation was performed on ice using modifications to manufacturer's guidelines. For CD90.1$^+$ cell isolation, 100 μL of rat serum and 50 μL of CD90.1$^+$ antibody cocktail was added to 2 mL of cell suspension and incubated on ice for 15 min, with vortex at 5 and 10 min. Following antibody incubation, 50 μL of magnetic beads were added and incubated on ice for 6 min (vortexing at 3 min). Cells were isolated on an EasySep magnet (2.5 min incubation, two 2 mL wash steps with ice-cold EasySep buffer). Isolated CD90.1$^+$ cells were resuspended in 1 mL of ice cold EasySep medium, filtered through a 0.75 μm filter to remove debris, and pelleted. For naive CD8$^+$ isolation, 100 μL of rat serum and 100 μL of naive antibody cocktail was added to 2 mL of cell suspension, followed by incubation on ice for 15 min. Following antibody incubation, 230 μL of magnetic beads were added, and cells incubated on ice for 6 min (vortexing at 3 min). The cell suspension was inserted into an EasySep magnet for 2.5 min, and the negative fraction (supernatant) collected in a fresh tube. Isolated cells (CD90.1$^+$ CD8$^+$ and naive CD8$^+$) were used immediately for Seahorse analysis, cultured for ex-vivo tracing, or flash-frozen for metabolomic and proteomic analysis.

QUANTIFICATION AND STATISTICAL ANALYSIS

Data are presented as mean ± SD for technical replicates or mean ± SEM for biological replicates and were analyzed using unpaired Student's t test or One-Way ANOVA. Statistical significance is indicated in all figures by the following annotations: *, $p < 0.05$; **, $p < 0.001$; ***, $p < 0.0001$. Further details of the number of replicates (n) for each experiment can be found in the figure legends.

DATA AND CODE AVAILABILITY

The published article includes all proteomics and metabolomics datasets generated and analyzed during this study. This study did not generate/analyze code.